Renata Lippi, Anita M. D, Angelo, Chaoen Li, Shaun C. Howard, Ian C. Madsen, Karen Wilson, Adam F. Lee, Christopher J. Sumby, Christian J. Doonan, Jim Patel, Danielle F. Kennedy

Unveiling the structural transitions during activation of a CO_2 methanation catalyst Ru^0/ZrO_2 synthesised from a MOF precursor

Catalysis Today, 2021; 368:66-77

Published at: http://dx.doi.org/10.1016/j.cattod.2020.04.043

Unveiling the structural transitions during activation of a CO_2 methanation catalyst Ru^0/ZrO_2 synthesised from a MOF precursor

Renata Lippi,*[1,2,3] Anita M. D'Angelo,[4] Chaoen Li,[3] Shaun C. Howard,[1] Ian C. Madsen,[5] Karen Wilson,[6] Adam F. Lee,[6] Christopher J. Sumby,[2] Christian J. Doonan,[2] Jim Patel,[3] Danielle F. Kennedy[1]

[1] CSIRO Manufacturing, Clayton VIC, Australia
[2] Department of Chemistry and Centre for Advanced Nanomaterials, The University of Adelaide, Adelaide SA, Australia
[3] CSIRO Energy, Clayton North VIC, Australia
[4] Australian Synchrotron, Clayton VIC, Australia
[5] CSIRO Minerals, Clayton VIC, Australia
[6] Applied Chemistry and Environmental Sciences, RMIT, Melbourne VIC, Australia
*Corresponding author: renata.lippi@csiro.au

Abstract

Carbon Capture, Utilisation and Storage (CCUS) technologies are utilised to minimise net CO_2 emissions and hence mitigate the impact of anthropogenic emissions on the global climate. One example of CO_2 utilisation is the production of carbon-neutral methane fuel via catalytic CO_2 reduction with H_2 (methanation). Thermal activation of a metal impregnated metal-organic framework (MOF), 1wt%Ru/UiO-66 in the presence of H_2 and CO_2 provides in situ synthesis of a highly active methanation catalyst: H_2 promotes the formation of Ru^0 nanoparticles, and CO_2 behaves as a mild oxidant to remove framework carbon and promote ZrO_2 crystallisation. The nature of the active MOF-derived Ru^0/ZrO_2 catalyst was studied by PXRD, TEM, and XAS, and the evolution of the parent 1wt%Ru/UiO-66 during thermal activation monitored in operando by synchrotron PXRD. The Ru impregnated Zr-based MOF collapses on heating in H_2 and CO_2 to form an amorphous C and Zr containing phase that subsequently crystallises as tetragonal (t-) ZrO_2 nanoparticles. These t-ZrO_2 nanoparticles undergo a subsequent phase transition to the more stable monoclinic (m-) ZrO_2 polymorph. In situ activation of Ru/UiO-66 generates a highly active catalyst for CO_2 methanation by transforming the MOF precursor into a (carbon-free) crystalline t-ZrO_2 support that stabilises highly dispersed metallic Ru nanoparticles. This insight may guide the rational design of future MOF-derived catalysts.

Keywords: MOF-derived catalyst; CO_2 methanation; in operando XRD; CO_2 conversion

1. Introduction

Rising anthropogenic CO_2 emissions and the consequent increase of atmospheric CO_2 concentrations is a significant environmental concern due to the associated impact on the global climate. In 2018, the Intergovernmental Panel on Climate Change (IPCC) published a special report entitled "Global warming of 1.5 °C", which highlighted the contribution of fossil fuel use to CO_2 emissions, and the need for a transition to renewable and low emissions technologies to limit the global temperature rise to 1.5 °C [1]. This shift away from traditional fossil energy sources and technologies will favour less carbon intensive options such as renewable energy (e.g. solar and wind), biofuels, electrification, advanced battery technologies and carbon capture, utilisation and storage (CCUS). Catalytic processes will play a critical role in many of these technologies, particularly for biofuels and CO_2 utilisation, for which new and improved catalysts may enable cost-effective pathways for marketable low-carbon fuels and chemicals. An attractive but challenging option is the conversion of atmospheric CO_2 into fuels (e.g. hydrocarbons and oxygenates). Although the combustion of such fuels will release CO_2 back to the atmosphere, the overall cycle has the potential to afford zero net CO_2 emissions. An important reason for considering such fuels is that they can be distributed and used with existing infrastructure, and thus have the potential to facilitate the transition to renewable energy resources.

The catalytic hydrogenation of CO_2 produces hydrocarbons and oxygenates depending on the process conditions and catalyst selected [2]. The hydrogenation of CO_2 to methane, generally known as CO_2 methanation or the Sabatier reaction, is a well-known process which typically proceeds with a high rate of CO_2 conversion and high selectivity for methane. The reaction takes place at elevated temperatures (300-400 °C) [3] and is highly exothermic (-165 kJ/mol CH_4). In industrial processes, CO_2 methanation catalysts are widely used to remove low concentrations of CO_2 from feed gases. The potential of CO_2 methanation for carbon-neutral fuel production has renewed interest in methanation catalyst development with a focus on catalytic activity and stability for concentrated CO_2 and H_2 feed streams.

Ruthenium, rhodium, nickel and cobalt are the main catalytic metals studied for CO_2 methanation [4, 5], and the lower cost of Ni makes it preferable for large-scale applications, although the high activity and stability of Ru catalysts can result in economic gains. Ru, Rh, Ni and Co catalysts are typically prepared by impregnation or co-precipitation on metal-oxides or zeolites, however these methods

offer limited control over the resulting metal morphology and distribution, and hence catalytic activity and stability. Catalyst supports, notably ZrO_2 and CeO_2, are demonstrated to directly participate in methanation through providing adsorption sites for CO_2 [6-9]. Synthetic methods are therefore required that provide good control over both metal and support to create well-defined active sites and reproducible catalyst performance.

Metal-organic frameworks (MOFs) are porous materials composed of inorganic nodes coordinated by organic linkers [10]. MOFs have been predominantly investigated for application to challenges in gas storage [11-15], gas separation [16-18], and catalysis [19-21]. Recently, MOF-derived materials have attracted significant attention, evidenced by recent reviews [22-29]. Specifically, the use of MOFs as sacrificial templates for functional materials has been shown to significantly impact the composition and morphology of the derived materials, and consequently improve their performance, particularly for electrochemistry [22, 24-26, 29] and catalysis [23, 24, 27-29]. Their intrinsic porosity and the potential to tailor their periodic structures (i.e. spacing between inorganic nodes) renders MOFs novel precursors for the synthesis of functional materials with complex and controlled compositions [30-32]. However, lack of a fundamental understanding of the “MOF-templating" or “MOF-derivation” mechanism is a limitation for the directed synthesis of new materials [22-29]. Efforts in this direction have been reported by Xu et al. who investigated the pyrolysis of a Ni-MOF into Ni^0 nanoparticles embedded in carbon by in situ TEM [33]. They observed the growth of Ni nanoparticles within a carbon matrix, the detachment of these nanoparticles from the matrix, and consequent agglomeration at higher temperatures. This knowledge enabled optimisation of the catalyst synthesis. In summary, understanding the mechanism of MOF-derivation is expected to enable the development of more sophisticated, tailored catalysts.

MOF-derivation is usually achieved via heat-treatment of the precursor MOF under inert (pyrolysis) or oxidising (calcination) atmospheres. Generally, pyrolysis yields metal, metal oxides or carbides nanoparticles embedded in a porous carbon matrix, whereas calcination leads to removal of carbon and the formation of metal oxide nanoparticles. Only a few reports have explored the use of reducing conditions (i.e. thermal treatment in H_2) in MOF-derivation [34, 35]. We previously reported a highly active Ru^0/ZrO_2 catalyst derived from a MOF subjected to CO_2 methanation conditions (80% H_2 and 20% CO_2 at 350 °C) [30]. This report exemplified the potential of using reducing atmospheres to synthesise metallic species from MOFs with controlled distribution and morphology. Here we

investigate the transformation of Ru/UiO-66 into an active CO_2 methanation catalyst by in operando PXRD. In addition, room temperature PXRD, TEM, XANES and EXAFS were also used to verify the nature of the MOF derived Ru^0/ZrO_2 catalyst.

2. Experimental

2.1 Synthesis of catalyst precursor

The precursor for the catalyst (MOF) described throughout this work is a post-synthetically modified (PSM) MOF achieved by the impregnation of a Zr-based MOF with $RuCl_3$ to produce 1wt% Ru loading on UiO-66. The Zr-based MOF, UiO-66, was synthesised based on the procedure described by Katz et al. [36], synthesis and impregnation details can be found in Lippi et al. [30]. In this manuscript 1wt%Ru/UiO-66 is simply referred to as MOF.

2.2 Heat-treatment

The MOF-derived catalysts (MDCs) were obtained after heat-treating the samples at 350 °C in different atmosphere compositions. Sample MDC_5H_2/N_2 was obtained by subjecting the MOF (1wt%Ru/UiO-66) to a heat-treatment under 5%H_2/N_2 gas flow using a tube furnace. The MOF sample was loaded into a quartz crucible and placed in a tube furnace. The upstream end was connected to a cylinder of 5% H_2 in N_2 and the downstream end connected to a bubbler, to ensure unidirectional flow. The samples were treated at 350 °C for 16 h under continuous gas flow (heating ramp rate set to 2 °C/min).

Reduction in a concentrated H_2 atmosphere (i.e. 80% H_2/N_2 or 80% H_2/CO_2) was carried out using the multi-channel catalyst testing rig described in the catalytic testing section. Specifically, 20 mg samples of MOF (Ru/UiO-66) were loaded in 4 different reactors. Reactor 1 and 2 were subjected to heat-treatment at 350 °C under a flow of 80%H_2/N_2 for 10 hours (Figure S1A), after that, reactor 1 was removed and the MOF-derived catalyst labelled "MDC_80H_2/N_2". Reactor 2 (pre-treated) remained in the rig and reactor 3 (fresh MOF) was added to it and these two samples were subjected to CO_2 methanation conditions for 30 hours (Figure S1B). The resulting samples in Reactors 2 and 3 were labelled "MDC_80H_2/N_2 + 80H_2/CO_2" and "MDC_80H_2/CO_2", respectively. Lastly, Reactor 4 was subjected to a long-term CO_2 methanation experiment at various temperatures, as described in Figure S1C, the used sample was labelled "MDC_80H_2/CO_2 long term".

2.1 Catalyst performance tests for CO_2 methanation

The catalytic performance testing was performed in a custom-built high-throughput catalyst testing rig, Flowrence^{TM} (Avantium, the Netherlands), described in Lippi et al. [30]. The rig is capable of simultaneously testing 48 fixed-bed microreactors that are distributed in 3 different blocks with independent temperature control. All reactors at a given time are subjected to identical conditions of gas flow, composition and pressure. In a typical experiment, 20 mg of sample mixed with 50 mg of SiC were loaded into quartz micro-reactors. The samples were first dried in pure N_2 at 200 °C (2 °C/min), then each reactor was exposed to reactive conditions: 2.47 sccm H_2, 0.65 sccm CO_2, 0.31 sccm Ar, 350 °C (5 °C/min) at 4 bar. For validation purposes, all experiments included positive and negative control samples.

2.2 Characterisation

2.2.1 Thermogravimetric analysis (TGA)

Residual carbon quantification was carried out by heating the samples to 700 °C under a constant flow of air (40 sccm) using a Perkin Elmer Pyris TGA. The effluent gas was analysed by a Pfeiffer Vacuum, ThermoStar GSD 320 T2 mass spectrometer.

2.2.2 Transmission electron microscopy (TEM)

TEM analysis was performed using a FEI Tecnai 12 G2 TEM operating at 120kV. High resolution TEM images were collected using a probe corrected JEOL ARM200F equipped with a cold field emission gun operating at 200 kV. The samples were prepared by suspension in ethanol and deposition on a holey carbon coated Cu grid.

2.2.3 Powder X-ray Diffraction (PXRD)

Synchrotron PXRD

Room temperature and in operando experiments were performed using the powder diffraction beamline at the Australian Synchrotron and used a Mythen-II strip detector [37] for pattern collection. Patterns were collected with 60 s of acquisition time at each of 2 different detector positions offset by 0.5° 2θ and later merged using PDViPeR to remove gaps in the datasets resulting from gaps between the detector modules. Phase identification was performed using the search and match algorithm in X'pert Highscore Plus (PANalytical, the Netherlands) [37]. The identified phases were quantified via

Rietveld refinement based quantitative phase analysis [38] using Topas V5 software (Bruker AXS, Germany) [39].

Room temperature PXRD

The powder samples were loaded in 0.7 mm glass capillaries (Charles Supper, USA) and rotated about the long capillary axis during room temperature acquisition. Synchrotron experiments were performed at 15, 16 and 17 keV (energy information corresponding to each pattern is in SI section 5.1).

In operando *PXRD*

For the in operando PXRD, a flow-through cell designed by the Australian Synchrotron was used and data was collected at 16 keV. The powder sample was loaded into open ended capillaries of outside diameter of 0.7 mm and wall thickness of 0.01 mm. Fibrous quartz glass wool was inserted into the exit of the capillary to prevent the sample being blown out by the applied gas flow. The capillary was mounted into the cell which was the fitted to the sample stage of the diffractometer. The gas inlet of the flow-through cell was connected to a gas mixing manifold using flexible nylon tubing. The gas manifold was connected to the capillary, pure N_2 and reactive gas mixture (25% CO_2 and 75% H_2). The sample was dried under a stream of N_2 while increasing the temperature to 200 °C at 10 °C/min. Upon reaching 200 °C, the sample was held at this temperature for 1 hour and then the gas feed switched to the reactive mixture of CO_2 and H_2. The temperature was varied according to the profile displayed in Figure 6B. This process broadly simulated the same activation and reaction conditions as those used in catalytic investigations. A flow meter was used to regulate the gas flow to 5 to 6 sccm for both N_2 and the reactive gas mixture. The cell was oscillated through 40° about the long capillary axis during data acquisition in order to maximise the number of crystallites contributing to the diffraction process and obtain the powder average. The gas outlet of the flow-through cell was connected to an OmniStar GSD 320 O2 mass spectrometer (MS) (Pfeiffer Vacuum GmbH, Germany) using flexible nylon tubing due to the oscillation of the flow-through cell. Heating of the capillary was achieved using a hot air blower and the temperature controlled and measured using a thermocouple positioned about 3 mm beneath the capillary. The hot air blower temperature was calibrated using 15 high temperature calibration samples under static atmosphere subjected to changing temperature from 100 °C to 700 °C, phase transitions were indicative of the real temperatures. Quantification was

carried out via Rietveld refinement using TOPAS V5 (Bruker AXS). Batch analysis for the quantification of the crystalline and amorphous phases is described in detail in SI section 5.2.

2.2.4 X-ray absorption

X-ray absorption (XAS) experiments at the Ru K-edge were undertaken at the XAS beamline of the Australian Synchrotron. The samples were diluted with cellulose powder to achieve a Ru loading of around 1000 ppm, the powders were then loaded onto room temperature stages. Next, they were scanned from 21.92 to 23.09 keV using fluorescence mode, and multiple patterns were collected for each sample. The acquired data was exported to ASC format using the software Sakura and later imported onto software Athena for merging multiple datasets, pre-edge subtraction, normalisation, XANES linear combination fitting and background subtraction to $\chi(k)$. The processed data was loaded onto software Artemis for EXAFS analysis. In addition to the samples of interest, the compounds Ru^0 foil, RuO_2 powder and $RuCl_3$ powder were also analysed and used as standards for linear combination fitting and for EXAFS comparison. For the EXAFS fitting, the amplitude reduction factor was obtained from fitting of Ru^0 foil and then applied for the EXAFS fitting of the MOF-derived catalyst sample. The fitting was performed with the input of two structures hexagonal-Ru^0 and tetragonal-RuO_2. The fitting was performed via least square methods considering a window of radial distance (R) specified in Table 2.

3. Results and Discussion

3.1 Effect of activation under H_2 atmosphere

The effect of a reducing atmosphere for catalyst activation on subsequent CO_2 methanation was investigated by comparing MOF-derived catalyst (MDC) samples obtained by pre-treatment at 350 °C in 5%H_2 in N_2 (label 5H2/N2) or 80% H_2 in N_2 (label 80H2/N2) with two MOF samples without any pre-treatment (Figure 1). Striking differences were observed for the sample pre-treated in 5%H_2/N_2 after 6 h on-stream, steady state H_2 conversion of 25.5% was observed, significantly lower than the other samples. CH_4 was the major gaseous product, although its average production of 7.4 mmol CH_4/g_{Ru}.min was lower than expected for the degree of H_2 and CO_2 conversion observed, suggesting carbon deposition on the catalyst. Trace amounts of CO (<0.05 mmol CO/g_{Ru}.min) were also detected during the first 30 h of the experiment. In contrast, activation occurred over the first 20 h of the experiment for the other three samples, evidenced by increased reactant conversion during this

period, followed by a steady H_2 conversion of 95%. These three samples were also 100% selective for methane with an excellent mass balance for CO_2/H_2 conversion and CH_4 production (no higher hydrocarbons were detected at any point).

These results suggest that a mild-reduction treatment (350 °C under 5%H_2/N_2) does not produce a highly active catalyst and in fact may result in coking. The catalyst pre-treated in 80%H_2/N_2 also underwent activation during CO_2 methanation (80% H_2/CO_2) similar to the precursor without any pre-treatment (Figure 1A inset). This activation step indicates that heat-treatment in a H_2-rich atmosphere is not sufficient to activate the MOF-derived catalyst. Furthermore, it suggests that CO_2 plays an important role in this catalyst activation. Pure UiO-66 treated in either 5%H_2 in N_2 or 80%H_2/CO_2 was inactive, confirming Ru as a key active catalytic component in the MOF-derived material.

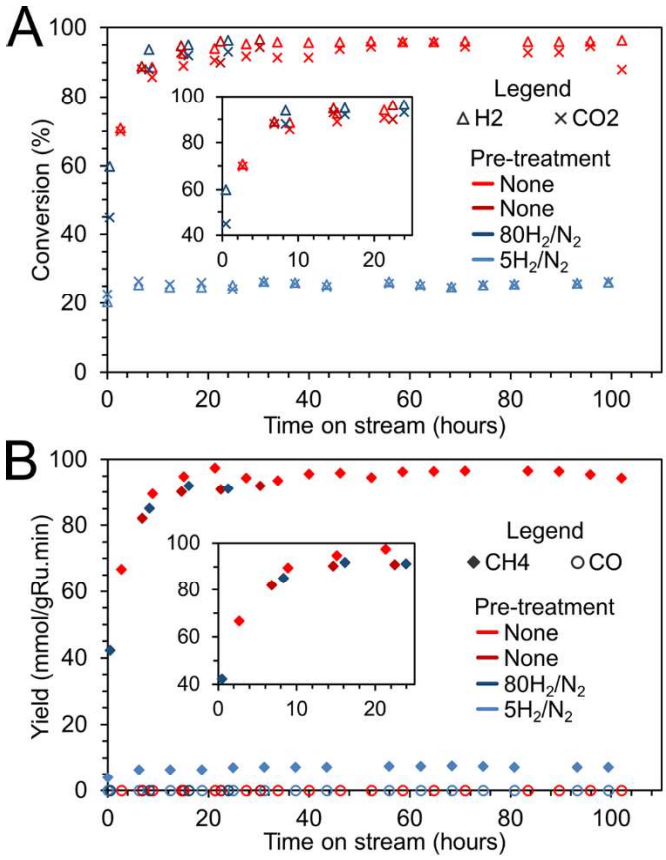

Figure 1: (A) H_2 and CO_2 conversion and (B) CH_4 and CO productivity during CO_2 methanation over as synthesised or H_2 pre-treated MOF(Ru/UiO-66) samples. Testing of the 80%H_2/N_2 (dark blue) pre-treated sample and one sample without pre-treatment (dark red) was limited to 30 h, whilst the other two samples remained on-stream for >100 h.

CO_2 methanation involves the following main reactions [40]:

$CO_2 + 4H_2 \rightarrow CH_4 + 2H_2O$, ΔH = -165 kJ/mol (1)

$CO_2 + H_2 \rightarrow CO + H_2O$, ΔH = +41 kJ/mol (2)

$CO + 3H_2 \rightarrow CH_4 + H_2O$, ΔH = -206 kJ/mol (3)

Reaction 2 is reversible and always occurs due to its lower activation energy barrier, and reaction 3 is usually fast [41], hence the overall methanation rate is determined by reaction 1 (either by direct conversion or hydrogenation of reactively-formed CO). Higher pressure favours reaction 1 [42], as observed for the MOF-derived catalyst (Figure 2B-D) under isothermal conditions. At 250 °C, the elevated pressure increased hydrogen conversion and methane production. Temperature also increased reactant conversion and selectivity (Figure 2A) up to 300 °C, suggesting that the reaction is kinetically controlled at lower temperature and reaches thermodynamic equilibrium above 300 °C.

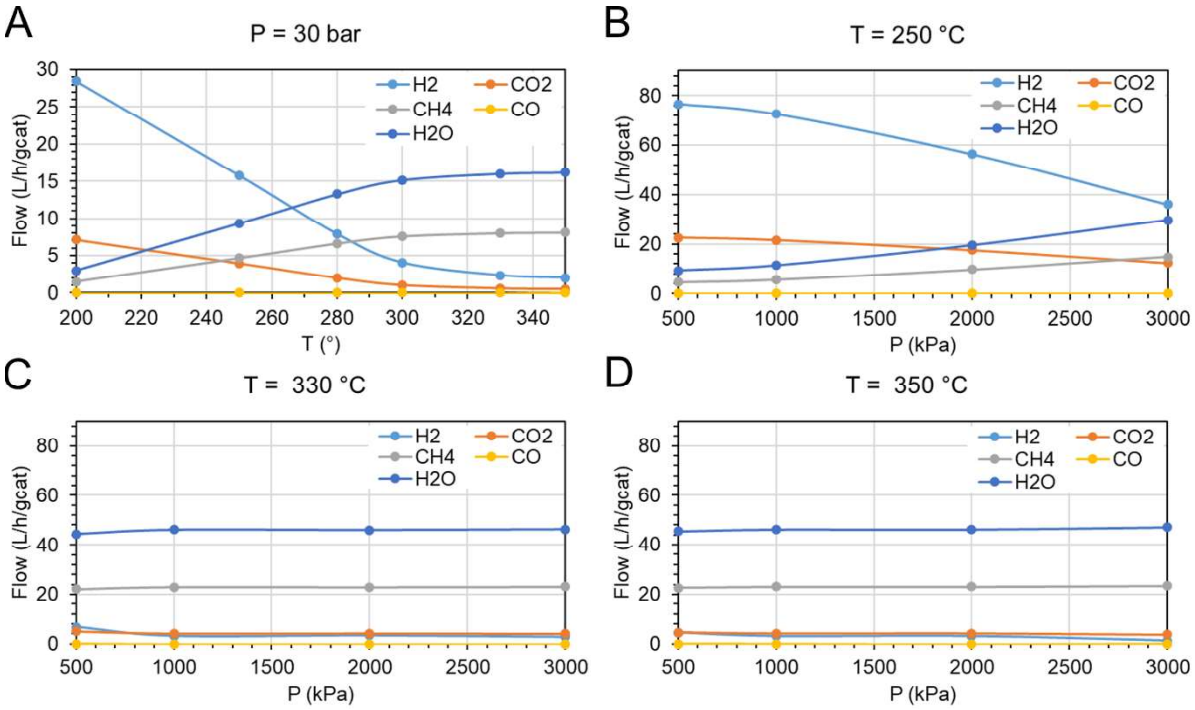

Figure 2: CO_2 methanation for MOF-derived catalyst activated at 80H2/CO2 as a function of reaction temperature and pressure: (A) at 30 bar; or at (B) 250 °C; (C) 330 °C; or (D) 350 °C.

3.2 Structural investigations

3.2.1 Room temperature PXRD

The preceding differences in catalytic behaviour with pre-treatment (5%H_2/N_2, 80%H_2/N_2 or 80%H_2/CO_2) were explored by TEM, XAS, and PXRD, the latter at room temperature and in operando

to establish the crystalline phases arising from the MOF precursor in situ. It is evident that the activation pre-treatment strongly influences the resulting crystallinity and phase (Figure 3).

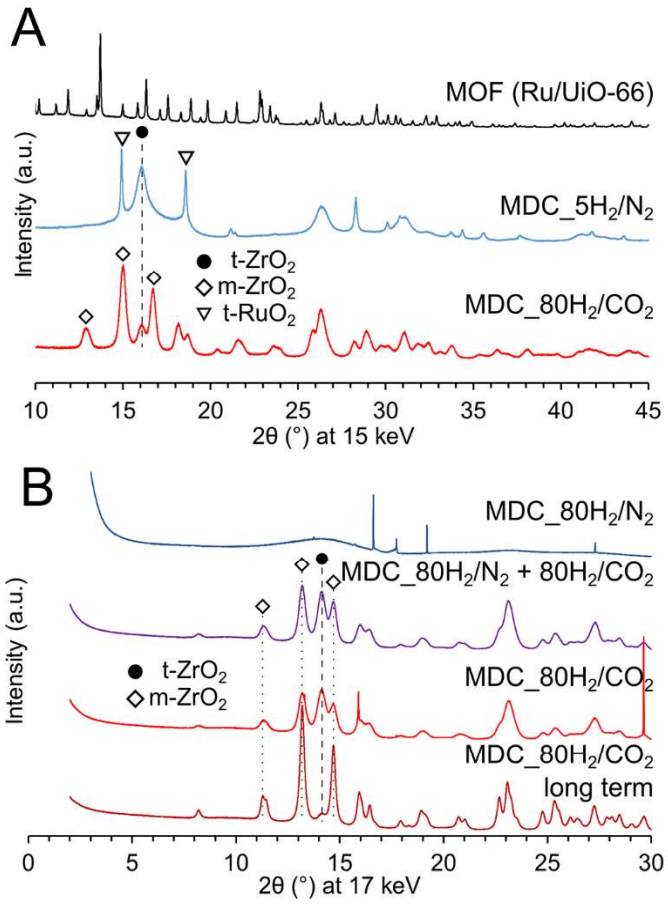

Figure 3: (A) PXRD patterns of the parent Ru/UiO-66 MOF, and resulting structures following thermal treatment in 5%H_2/N_2 (MDC_5H_2/N_2) and 100 h methanation reaction (MDC_80H_2/CO_2). (B) Samples derived from MOF after thermal treatment in either 80%H_2/N_2, 80%H_2/CO_2, or both sequentially. Crystalline phases are indicated by symbols; unlabelled sharp peaks are SiC diluent.

Table 1: Rietveld refinement quantitative phase analysis and crystallite size (LvolIB) for the PXRD patterns in Figure 3.

Samples	Atmosphere composition	Time (h)	UiO-66		*t*-ZrO_2		*m*-ZrO_2		*t*-RuO_2	
			wt%	LvolIB (nm)	wt%	LvolIB (nm)	wt%	LvolIB (nm)	wt%	LvolIB (nm)
MOF	-	-	100	112	-	-	-	-	-	-
MDC_5H_2/N_2	5% H_2/N_2	16	-	-	87.7	9.9	-	-	12.3	43
MDC_80H_2/N_2	80% H_2/N_2	10	- [a]	-	- [a]	-	- [a]	-	- [a]	-
MDC_80H_2/N_2 + 80H_2/CO_2	80% H_2/N_2	10	-	-	32.6	11.8	67.4	14.3	-	-
	80% H_2/CO_2	30								
MDC_80H_2/CO_2	80% H_2/CO_2	30[b]	-	-	33.8	11.3	66.2	13.4	-	-

MDC_80H_2/CO_2	80% H_2/CO_2	100[c]	-	-	16.0	7.7	84.0	10	-	-
MDC_80H_2/CO_2 long term	80% H_2/CO_2	250	-	-	4.6	10.3	95.5	22.3	-	-

All MDC samples were treated at 350°C; [a] amorphous phase; [b] diffractogram displayed in Figure 3B; [c] diffractogram displayed in Figure 3A.

Mild reducing conditions (MDC_5H_2/N_2) resulted in the emergence of t-ZrO_2 and RuO_2 reflections (Figure 3A), with quantitative phase analysis (QPA) by Rietveld refinement [38] indicating a composition of 87.7wt% t-ZrO_2 and 12.3wt% RuO_2. Comparison with the 1wt%Ru/UiO-66 precursor implies the RuO_2 content is overestimated, attributed to the presence of amorphous C and Zr containing phases. The carbon content was therefore quantified by temperature-programmed oxidation (TPO), which revealed the presence of 32 wt% carbon in MDC_5H_2/N_2 (Figure S3B). The poor catalytic performance of this materials is explained by the presence of large (43 nm) RuO_2 crystallites and heavy coking. Subsequent reduction of such RuO_2 particles during CO_2 methanation conditions would likely produce Ru^0 particles of similar size [43] and hence low surface area and activity. Mild reduction in 5%H_2/N_2 induces collapse of the MOF crystalline framework but does not remove the resulting fragments of organic linkers. We propose that site-blocking by this residual amorphous carbon phase, in conjunction with the formation of large RuO_2 particles, accounts for the poor methanation performance observed.

More reducing conditions (MDC_80H_2/N_2) result in only broad amorphous bands and sharp SiC peaks (the catalyst diluent during reactivity tests). The broad peaks agree with the expected reflections for m-ZrO_2 and t-ZrO_2, and are not due to background contribution from the quartz capillary. This amorphous material comprises a mixture of MOF breakdown products: amorphous carbon, and Ru and Zr phases; TPO revealed 16.6 wt% of carbon remnant (Figure S3C). As indicated by the catalytic tests in Figure 1, this sample differs significantly from that obtained by mild reduction (MDC_5H_2/N_2), being amorphous and not exhibiting RuO_2 features. Although hydrogen-rich treatment alone is insufficient to form the (highly active) metallic Ru catalyst observed during methanation [30], attendant formation of an amorphous and carbon-rich state does not inhibit later transformation into the active catalyst state on subsequent exposed to methanation conditions (80%H_2 in CO_2).

Thermal processing in the presence of CO_2 appears essential to produce the crystalline ZrO_2 observed in the highly active catalysts, as seen by comparing the PXRD patterns of the MOF treated in 80%H_2 in N_2 (MDC_80H_2/N_2) versus that first treated in 80%H_2 in N_2 and subsequently in 80%H_2 in CO_2 during CO_2 methanation (MDC_80H_2/N_2 + 80H_2/CO_2). The latter material exhibited little

difference from that of the MOF directly subjected to 80%H_2 in CO_2 (MDC_80H_2/CO_2), and containing <2wt% carbon following the first activation step (Figure S3D). Heating in CO_2 is reported to selectively etch carbon nanotubes, acting as a mild oxidant compared to oxygen or air [44]. We therefore hypothesise that CO_2 acts as a mild oxidant of the MOF, combusting organic linker fragments and supplying oxygen to promote ZrO_2 the crystallisation. In tandem, H_2 promotes structural decomposition of the MOF and the reduction of liberated Ru^{x+} to Ru metal (and maintains it in a reduced state).

Catalyst activation under CO_2 methanation conditions (MDC_80H_2/CO_2) yielded a mixture of m- and t-ZrO_2 phases. PXRD patterns revealed no reflections attributable to Ru phases (Ru^0 or RuO_2), consistent with the formation of highly dispersed Ru nanoparticles; the nature and size of these particles is discussed in the following sections. Monoclinic ZrO_2 is the thermodynamically stable polymorph, converting to tetragonal at ~1188 ºC [45] and to cubic at 2311 ºC [46]. Catalytic activity varies among the polymorphs, with t-ZrO_2 reported to be more active than m-ZrO_2 for CO_2 methanation [47-49]. The tetragonal polymorph has been observed as a product of UiO-66 thermal decomposition [50].Tetragonal ZrO_2 can be stabilised at room temperature either by doping or the formation of a nanocrystalline powder with crystallites below a 'critical size'. This critical size varies from 3.7 nm to 29.5 nm depending on the synthesis conditions and nanocrystal morphology [51, 52]. Reports suggest that the monoclinic phase forms by coarsening of the tetragonal polymorph, so the crystallite size of m-ZrO_2 is expected to exceed that of t-ZrO_2 [52] in agreement with our observations (Figure 3). The mass ratio of monoclinic:tetragonal ZrO_2 increases with time on-stream for MDC_80H_2/CO_2, from 66:34 after 30 h, to 84:16 after 100 h and then 95:5 after 250; this confirms the progressive evolution from t-ZrO_2 to the m-ZrO_2 for the active catalyst. The subsequent formation of the monoclinic phase does not have a detrimental effect to the catalytic activity.

3.2.2 TEM

TEM of the MOF, MDC_5H_2/N_2, and MDC_80H_2/CO_2 samples (Figure 4) demonstrates the similarity between the MOF and MDC_5H_2/N_2, and the differences between these samples and the highly active catalyst (MDC_80H_2/CO_2). The observation of translucent particles in Figure 4A is attributed to their low electron density and a consequence of narrow particle thickness, single crystal orientation and/or the presence of light elements (C, O and H) which comprise the MOF organic linkers. TPO was undertaken to quantify the carbon content, and confirmed as 48 wt%, 32 wt% and <2wt% for the

MOF, MDC_5H_2/N_2 and MDC_80H_2/CO_2, respectively. The similar morphology and carbon content for both the MOF and MDC_5H_2/N_2 particles, demonstrate that linker decomposition products persist after thermal treatment in a mild reducing atmosphere, consistent with the presence of an amorphous carbon phase inferred from PXRD. The activated catalyst MDC_80H_2/CO_2 is composed of clusters of electron-dense <30 nm nanoparticles, which we assigned to the ZrO_2 crystallites identified by PXRD.

HR-TEM investigations were conducted on the catalyst synthesised in situ under catalytic CO_2 methanation conditions (MDC_80H_2/CO_2) to investigate the nature of the Ru phase. The presence of Ru nanoparticles has been previously confirmed by high magnification EDS mapping of catalysts formed under these conditions [30]. Here, HR-TEM investigations revealed 2 to 5 nm Ru^0 nanoparticles (Figure 4D and 4E), which were not observable by PXRD. The presence of such small and monodispersed Ru^0 nanoparticles (and hence high area of active metal) is hypothesised to promote the high methanation activity of this catalyst. The presence of lattice fringes indicates the presence of some single crystal Ru^0 nanoparticles, whereas others appear disordered or amorphous in nature, which could be an artefact of particle orientation under the beam; the relative contributions of crystalline versus amorphous Ru particles to CO_2 methanation requires future experimental and computational study.

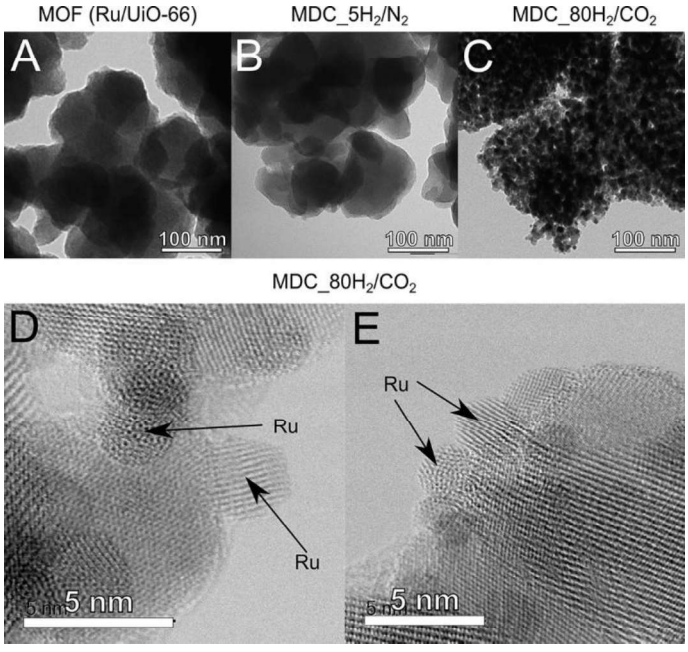

Figure 4: TEM of (A) MOF, (B) MDC_5H_2/N_2, and (C) MDC_80H_2/CO_2; and (D, E) High Resolution TEM images of MDC_80H_2/CO_2. The arrows indicate Ru^0 nanoparticles.

3.2.3 X-ray absorption near edge structure (XANES)

The local chemical environment of Ru within these nanoparticles was subsequently studied by XAS. Ru K-edge X-ray absorption near edge structure (XANES) spectra (Figure 5A) of the MOF-derived catalyst (MDC_80H_2/CO_2) and in its precursor (MOF), and semi-quantitative linear combination fitting to Ru foil, RuO_2 and $RuCl_3$ standards (Figure S4) reveals mostly metallic Ru in MDC_80H_2/CO_2 (62% Ru^0 and 38% RuO_2), whereas that in the MOF was mostly tetravalent (78.3% RuO_2, 14% $RuCl_3$ and 7.7% Ru^0). Conversion of the MOF to the highly active methanation catalyst is therefore accompanied by the reduction of Ru^{4+} to Ru^0. Residual oxidic Ru in the activated catalyst may reflect either partial re-oxidation of Ru atoms in the surface of metal nanoparticles on air exposure prior to the analysis, or the interaction of Ru with O atoms on the ZrO_2 support interface. XANES evaluation of the catalyst precursor (MOF), which is prepared by the impregnation of a Zr-MOF with $RuCl_3$, reveals that once Ru is impregnated it is no longer in its chloride-bound form. These findings also support our previous DFT studies which suggested that Ru can be dispersed throughout the MOF by binding to the inorganic node $Zr_6O_4(OH)_4$ of UiO-66 at sites missing an organic linker [30]. Our UiO-66 synthesis method uses HCl as a modulator, which may also increase the number of such “missing linker” defects [53]. Creation of a large number of such defect related binding sites would promote a high level of Ru atom dispersion throughout the MOF. Ru bound to two oxygen atoms in such a defect configuration would appear structurally similar to RuO_2.

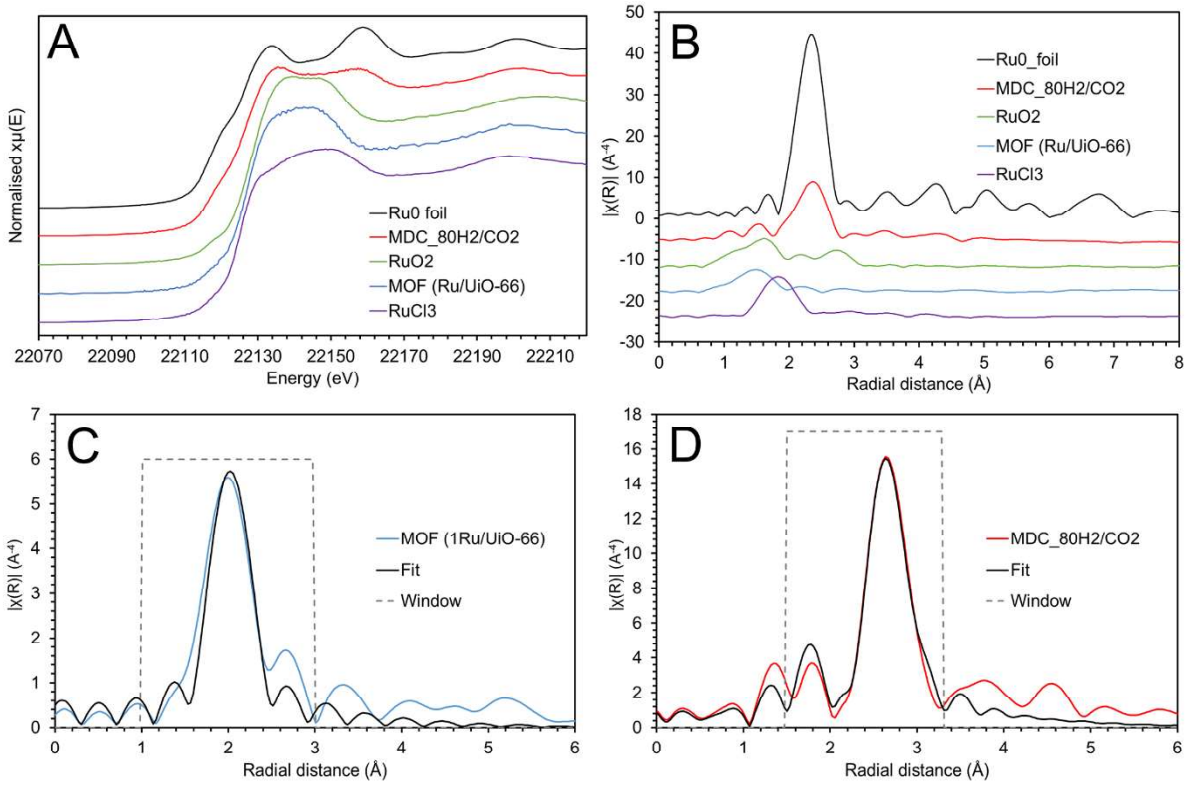

Figure 5: (A) XANES spectra and (B) k^3-weighted Fourier-transform EXAFS spectra for used catalyst MDC_80H_2/CO_2, its precursor MOF and standards Ru^0 foil, RuO_2 and $RuCl_3$; Phase-corrected Fourier transform radial-distribution function and fits for (C) the catalyst precursor MOF and (D) the highly active catalyst MDC_80H_2/CO_2.

3.2.4 Extended X-ray absorption fine structure (EXAFS)

The structural environment of Ru in the MOF and resulting MOF-derived catalyst MDC_80H_2/CO_2 was investigated by Ru K-edge EXAFS. The Fourier-transform of the catalyst shows an intense shell at 2.68 Å arising from Ru-Ru contributions and a Ru-O shell ~2.00 Å (Figure 5D and Table 2). The fitted Ru-Ru coordination number (CN) of 6.5 is significantly lower than that obtained for Ru^0 foil (CN=12), in agreement with the high number of coordinatively unsaturated atoms expected for 2 to 5 nm Ru nanoparticles. The small Debye-Waller factor (σ^2) for the Ru-Ru shell suggests that the Ru^0 nanoparticles are highly ordered [54], and hence mainly in crystalline rather than amorphous form. The Ru-O CN of 2.36 is significantly lower than expected for bulk RuO_2 (CN=6) consistent with the presence of a truncated surface oxide or interaction of Ru nanoparticles with the metal oxide support.

The Ru/UiO-66 MOF precursor exhibited a Ru-O shell at 2.03 Å (Figure 5C and Table 2) similar to that in bulk RuO_2 and inconsistent with the spectra of $RuCl_3$ or Ru metal (Figure 5B). This Ru-O scattering distance is in good agreement with our previous DFT calculations which predicted Ru-O distances of 2.0 and 2.1 Å for Ru binding to the MOF node in the missing linker configuration [30]. Incipient wetness impregnation may therefore produce a MOF with Ru integrated in the framework which likely accounts for the high dispersion of Ru in the catalyst precursor and subsequent genesis of small Ru metal nanoparticles on activation under methanation conditions.

Table 2: Ru K-edge EXAFS fitted parameters.

sample	shells	Fitting Range (A)	Coordination number	σ^2	R(A)	Delta E0 (eV)	R-factor (%)
MDC_80H_2/CO_2	Ru-Ru	1.5-3.3	6.5 ± 1.3	0.00475	2.68	-3.80 ± 1.29	1.58%
MDC_80H_2/CO_2	Ru-O	1.5-3.3	2.4 ± 1.8	0.00384	2.00	-3.80 ± 1.29	1.58%
MOF (Ru/UiO-66)	Ru-O	1-3	4.8 ± 1.4	0.00485	2.03	0.50 ± 3.84	7.49%
Ru^0 Foil	Ru-Ru	1.5-3.3	12	0.00315	2.67	-5.38 ± 1.05	1.85%

3.2.5 In operando PXRD

The phase transition the MOF undergoes on exposure to the CO_2 methanation reaction conditions was studied in operando. The aim was to elucidate the structural properties of the MOF-derived catalyst that lead to its exceptional catalytic activity and the role of the precursor MOF in achieving this structure. The catalyst precursor (MOF) was subjected to simulated CO_2 methanation conditions in a controlled atmosphere and variable temperature PXRD experiment. Over 700 patterns were collected over 33 hours of experiment, representative patterns are displayed in Figure 6A. The temperature profile during the experiment is shown in Figure 6B and the numbers indicate changes during the experiment. These are described in Table S4 together with our observations.

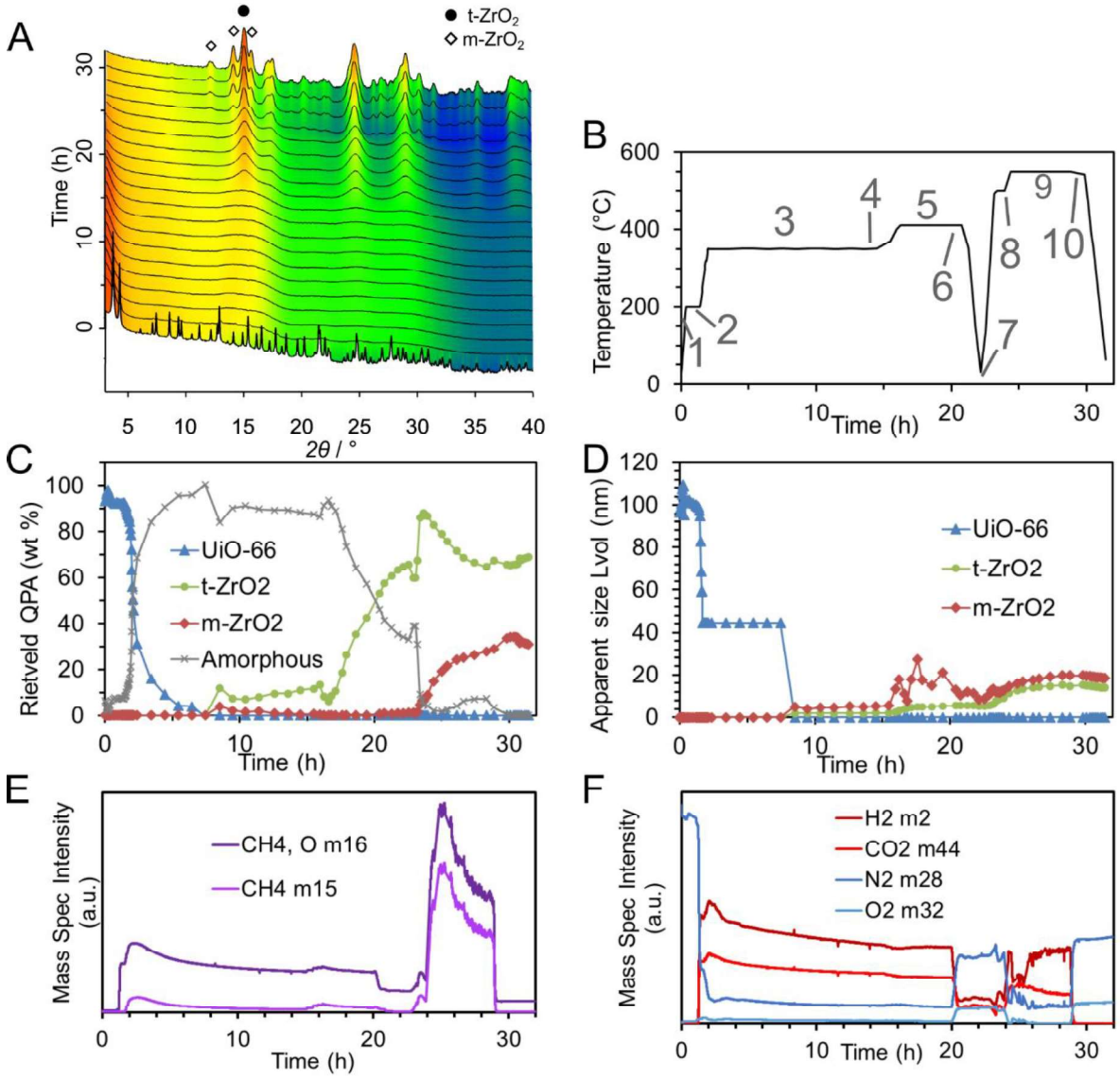

Figure 6: (A) 3D stacked data view of PXRD patterns offset; (B) temperature profile during the experiment, numbers indicate events and observations described in Table S4; (C) quantitative phase analysis (details in SI); (D) apparent size (LvolIB); (E) CH_4 production by mass spectrometry; and (E) H_2, CO_2, N_2 and O_2 analysis by mass spectrometry.

Upon heating the sample under the flowing gas mixture (75% H_2 and 25% CO_2), the crystalline MOF structure collapsed at ~330 °C producing an amorphous phase. The amorphous material remained stable at 350 °C for 8 hours with no formation of ZrO_2 or Ru phases. A difference between the set and the real temperature of 100-200 °C was inferred by comparison with the catalytic performance

observed in a conventional reactor. This difference can be explained by the heat-transfer to the cold gas flowing through the sample (SI section 5.3).

As noted, the MOF structure is stable at low temperatures under the H_2/CO_2 mixture but collapses at 330 °C (set temperature) with the release of different organic fragments. The remaining solid is amorphous causing an increased contribution to the background of the patterns. This amorphous contribution to the patterns was quantified by modelling the background increase via indirect quantitative phase analysis (QPA) via Rietveld refinement (details in SI). The QPA demonstrated that the amorphous phase is stable for over 10 h at 350 °C (set temperature). We note that this phase was inactive for CH_4 production (Figure 6F). Upon increasing the temperature, the amorphous phase undergoes a transition to form ZrO_2 nanoparticles. Initially t-ZrO_2 is formed and the catalyst begins to show moderate CH_4 production. At even higher temperatures, m-ZrO_2 is formed in addition to t-ZrO_2 and the amorphous phase is no longer observed. The increase in temperature also caused the growth of the crystallite sizes although they remained below 20 nm throughout the duration of this experiment, which is considerably smaller than the crystallite size of the precursor MOF. Upon growth of ZrO_2 nanocrystals, the catalytic production of CH_4 experienced a 5-fold increase compared to the activity of the amorphous phase. Even though ZrO_2 is not the catalytically active phase, a direct correlation between the high catalytic activity and the formation of ZrO_2 nanoparticles was observed. This is explained by the role that removal of amorphous carbon has on promoting formation of ZrO_2. The newly formed t-ZrO_2 particles act as a support for the immobilisation of Ru nanoparticles. Once Ru binds to t-ZrO_2, the strong Ru-O bond inhibits Ru mobility and consequently limits Ru nanoparticle agglomeration. Growth of t-ZrO_2 particles lead to m-ZrO_2, and this phase transition does not significantly affect the mobility of Ru nanoparticles given the bond strength in monoclinic and tetragonal are comparable [56]. Therefore, the use of a Ru-impregnated MOF as the catalyst precursor was key to provide a framework with excellent distribution control of both Zr and Ru. Upon collapse of this framework, the proximity of the two elements led to the stabilisation of Ru atoms by t-ZrO_2 seeds. These seeds initially embed in an amorphous carbon phase, then coarsen and transition to m-ZrO_2. Ru^0 nanoparticles that were formed under the highly reducing atmosphere were stabilised by the interaction with the support and remained in a size range below the PXRD detection limit. This in operando PXRD experiment has elucidated the structural transition that the MOF undergoes during CO_2 methanation to form the active catalyst. These findings demonstrate the complexity of the

transformations undertaken by the catalyst and the synergistic effect of an atmosphere with both H_2 and CO_2, and are key for the rational design of new structures derived from MOFs.

4. Conclusion

In summary, we have investigated a protocol for MOF-derived catalyst activation using a combination of H_2 and CO_2 at 350 °C to produce a nanostructured Ru^0/ZrO_2 catalyst with high activity for CO_2 methanation. In this investigation, activation in two concentrations of H_2 diluted in N_2 were compared to the in situ activation protocol (Scheme 1A). A low concentration of H_2 (5%H_2 in N_2) during the heat-treatment of Ru/UiO-66 was found to be detrimental to the synthesis of a highly active catalyst. Specifically, the diluted H_2 atmosphere promoted the synthesis of large RuO_2 nanoparticles (43 nm) and amorphous carbon, which account for the poor catalytic performance (25% CO_2 conversion). A high concentration of H_2 (80% H_2 in N_2) caused the collapse of the MOF-framework into an amorphous mixture of MOF-breakdown products containing carbon, ruthenium and zirconium phases. This highly reducing atmosphere was not sufficient for the activation of the catalyst, which is only activated after 20 hours under CO_2 methanation conditions. Once activated, the catalyst has nearly identical performance and structure to the catalyst derived from directly subjecting a pristine MOF sample to CO_2 methanation conditions; both samples displayed CO_2 conversion of 95%. These results highlight the synergistic role of the H_2 and CO_2 mixture for the synthesis of the nanostructured Ru^0/ZrO_2 catalyst: H_2 acts by breaking down the MOF framework and by reducing Ru atoms; whilst CO_2 acts as a mild oxidant promoting the removal of carbon. This combination ensures the synthesis of Ru^0 nanoparticles dispersed through the material during the crystallization of ZrO_2 nanoparticles. Ruthenium is likely present in the catalyst precursor Ru/UiO-66 bound to the inorganic node of the MOF structure in “missing linker” defects, which would ensure excellent dispersion of Ru in the sample and proximity to Zr and O atoms. The phase transitions during the catalyst activation in H_2/CO_2 mixture were elucidated by an in operando PXRD experiment. This experiment demonstrated that the crystalline MOF structure collapses into an amorphous phase due to the highly reducing atmosphere and increasing temperatures. This amorphous phase is stable at lower temperatures, but at higher temperatures the oxidant effect of CO_2 promotes the removal of carbon and the formation of *t*-ZrO_2 nanoparticles, supporting Ru^0 and promoting high catalytic activity for the catalyst. Through coarsening of the t-phase, m-ZrO_2 is formed (Scheme 1B). Notably, the formation of m-ZrO_2 is not detrimental to the catalyst as long-term tests showed stable catalytic activity is achieved with 84 to

95% m-ZrO_2. These combined experiments illustrate the delicate interplay of factors in the MOF-derivation process and moreover, the value of employing reducing conditions, with an additional mild oxidant, for converting a MOF template to a highly active catalyst.

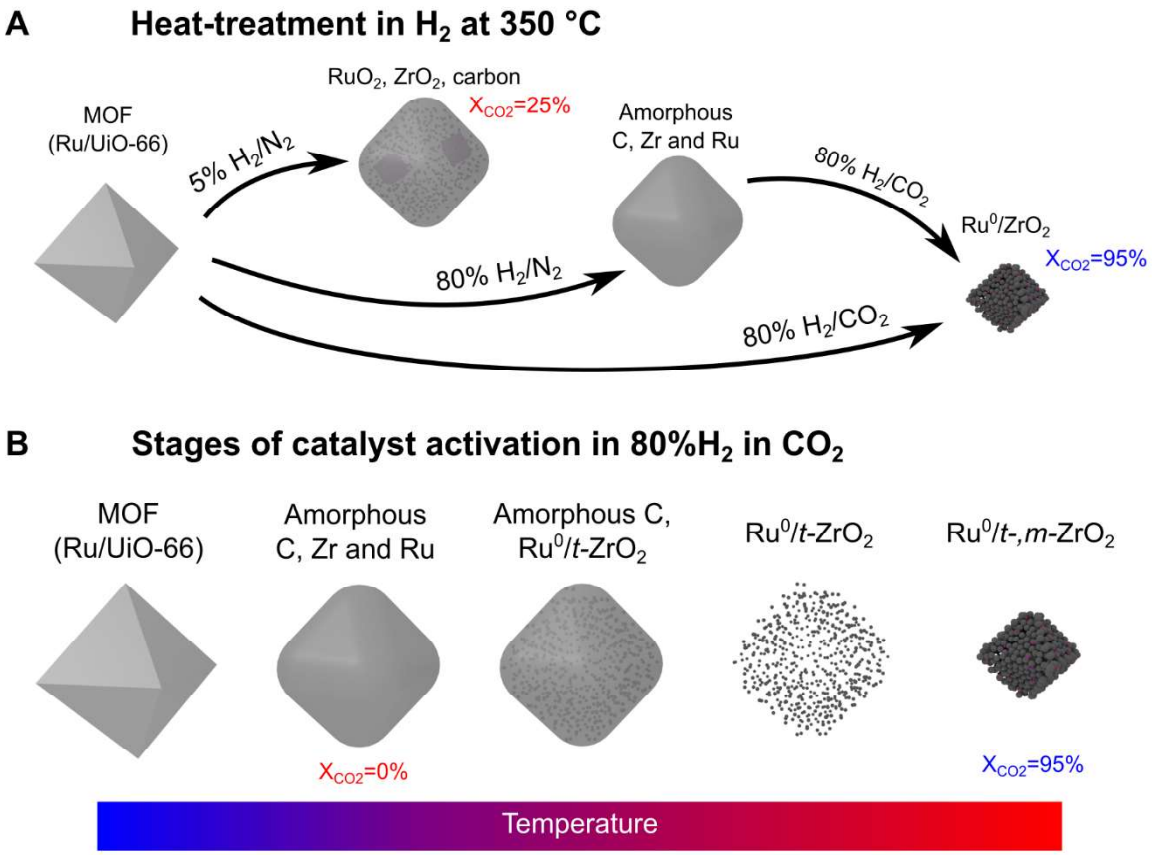

Scheme 1: (A) MOF-derived materials according to the atmosphere composition during thermal-treatment. (B) Phase transition during MOF-derivation during CO_2 methanation reaction conditions.

5. Acknowledgements

The authors would like to acknowledge Yunxia Yang for assisting with TGA experiments, Jiajia Zhao and Daksh Shah for assistance during Synchrotron experiments, and the CSIRO characterisation group for TEM experiments. This work was supported by the CSIRO Active Integrated Matter Future Science Platform and the Science and Industry Endowment Fund. Aspects of this work were undertaken at the Australia Synchrotron at the Powder Diffraction (proposals M11125 and EU15969) and X-ray Absorption beamlines (proposal M14282). RL acknowledges the University of Adelaide for

the Beacon of Enlightenment PhD Scholarship and the CSIRO Active Integrated Matter Future Science Platform for the FSP Postdoctoral Fellowship.

6. References

[1] IPCC, Summary for Policymakers, in: V. Masson-Delmotte, P. Zhai, H.O. Pörtner, D. Roberts, J. Skea, P.R. Shukla, A. Pirani, W. Moufouma-Okia, C. Péan, R. Pidcock, S. Connors, J.B.R. Matthews, Y. Chen, X. Zhou, M.I. Gomis, E. Lonnoy, T. Maycock, M. Tignor, T. Waterfield (Eds.) Global warming of 1.5°C, 2018.

[2] K. Ahmad, S. Upadhyayula, Greenhouse gas CO2 hydrogenation to fuels: A thermodynamic analysis, Environ. Prog. Sustain,, 38 (2019) 98-111.

[3] W. Li, H. Wang, X. Jiang, J. Zhu, Z. Liu, X. Guo, C. Song, A short review of recent advances in CO2 hydrogenation to hydrocarbons over heterogeneous catalysts, RSC Adv., 8 (2018) 7651-7669.

[4] P. Frontera, A. Macario, M. Ferraro, P. Antonucci, Supported Catalysts for CO2 Methanation: A Review, Catalysts, 7 (2017).

[5] J. Gao, Q. Liu, F. Gu, B. Liu, Z. Zhong, F. Su, Recent advances in methanation catalysts for the production of synthetic natural gas, RSC Adv., 5 (2015) 22759-22776.

[6] W. Li, X. Nie, X. Jiang, A. Zhang, F. Ding, M. Liu, Z. Liu, X. Guo, C. Song, ZrO2 support imparts superior activity and stability of Co catalysts for CO2 methanation, Appl. Catal., B, 220 (2018) 397-408.

[7] Y. Guo, S. Mei, K. Yuan, D.-J. Wang, H.-C. Liu, C.-H. Yan, Y.-W. Zhang, Low-Temperature CO2 Methanation over CeO2-Supported Ru Single Atoms, Nanoclusters, and Nanoparticles Competitively Tuned by Strong Metal–Support Interactions and H-Spillover Effect, ACS Catal., 8 (2018) 6203-6215.

[8] X. Wang, L. Zhu, Y. Liu, S. Wang, CO2 methanation on the catalyst of Ni/MCM-41 promoted with CeO2, Sci. Total Environ., 625 (2018) 686-695.

[9] H. Takano, Y. Kirihata, K. Izumiya, N. Kumagai, H. Habazaki, K. Hashimoto, Highly active Ni/Y-doped ZrO2 catalysts for CO2 methanation, Appl. Surf. Sci., 388 (2016) 653-663.

[10] S.R. Batten, N.R. Champness, X.M. Chen, J. Garcia-Martinez, S. Kitagawa, L. Ohrstrom, M. O'Keeffe, M.P. Suh, J. Reedijk, Terminology of metal-organic frameworks and coordination polymers (IUPAC Recommendations 2013), Pure Appl. Chem., 85 (2013) 1715-1724.

[11] K. Sumida, D.L. Rogow, J.A. Mason, T.M. McDonald, E.D. Bloch, Z.R. Herm, T.-H. Bae, J.R. Long, Carbon Dioxide Capture in Metal–Organic Frameworks, Chem. Rev., 112 (2011) 724-781.

[12] M.P. Suh, H.J. Park, T.K. Prasad, D.-W. Lim, Hydrogen Storage in Metal–Organic Frameworks, Chem. Rev., 112 (2011) 782-835.

[13] Y. Peng, V. Krungleviciute, I. Eryazici, J.T. Hupp, O.K. Farha, T. Yildirim, Methane Storage in Metal–Organic Frameworks: Current Records, Surprise Findings, and Challenges, J. Am. Chem. Soc., 135 (2013) 11887-11894.

[14] J.A. Mason, M. Veenstra, J.R. Long, Evaluating metal-organic frameworks for natural gas storage, Chem. Sci., 5 (2014) 32-51.

[15] Y. He, W. Zhou, G. Qian, B. Chen, Methane storage in metal-organic frameworks, Chem. Soc. Rev., 43 (2014) 5657-5678.

[16] J.-R. Li, J. Sculley, H.-C. Zhou, Metal–Organic Frameworks for Separations, Chem. Rev., 112 (2011) 869-932.

[17] B. Van de Voorde, B. Bueken, J. Denayer, D. De Vos, Adsorptive separation on metal-organic frameworks in the liquid phase, Chem. Soc. Rev., 43 (2014) 5766-5788.

[18] Z. Kang, L. Fan, D. Sun, Recent advances and challenges of metal-organic framework membranes for gas separation, J. Mater. Chem. A, 5 (2017) 10073-10091.

[19] J. Lee, O.K. Farha, J. Roberts, K.A. Scheidt, S.T. Nguyen, J.T. Hupp, Metal-organic framework materials as catalysts, Chem. Soc. Rev., 38 (2009) 1450-1459.

[20] J. Liu, L. Chen, H. Cui, J. Zhang, L. Zhang, C.-Y. Su, Applications of metal-organic frameworks in heterogeneous supramolecular catalysis, Chem. Soc. Rev., 43 (2014) 6011-6061.

[21] P. Garcia-Garcia, M. Muller, A. Corma, MOF catalysis in relation to their homogeneous counterparts and conventional solid catalysts, Chem. Sci., 5 (2014) 2979-3007.

[22] W. Xia, A. Mahmood, R. Zou, Q. Xu, Metal-organic frameworks and their derived nanostructures for electrochemical energy storage and conversion, Energy Environ. Sci., 8 (2015) 1837-1866.

[23] Y. Song, X. Li, L. Sun, L. Wang, Metal/metal oxide nanostructures derived from metal-organic frameworks, RSC Adv., 5 (2015) 7267-7279.

[24] K. Shen, X. Chen, J. Chen, Y. Li, Development of MOF-Derived Carbon-Based Nanomaterials for Efficient Catalysis, ACS Catal., 6 (2016) 5887-5903.

[25] X. Cao, C. Tan, M. Sindoro, H. Zhang, Hybrid micro-/nano-structures derived from metal-organic frameworks: preparation and applications in energy storage and conversion, Chem. Soc. Rev., 46 (2017) 2660-2677.

[26] Z. Xie, W. Xu, X. Cui, Y. Wang, Recent Progress in Metal–Organic Frameworks and Their Derived Nanostructures for Energy and Environmental Applications, ChemSusChem, 10 (2017) 1645-1663.

[27] S.-N. Zhao, X.-Z. Song, S.-Y. Song, H.-j. Zhang, Highly efficient heterogeneous catalytic materials derived from metal-organic framework supports/precursors, Coord. Chem. Rev., 337 (2017) 80-96.

[28] L. Oar-Arteta, T. Wezendonk, X. Sun, F. Kapteijn, J. Gascon, Metal organic frameworks as precursors for the manufacture of advanced catalytic materials, Mater. Chem. Front., 1 (2017) 1709-1745.

[29] Y.V. Kaneti, J. Tang, R.R. Salunkhe, X.C. Jiang, A.B. Yu, K.C.W. Wu, Y. Yamauchi, Nanoarchitectured Design of Porous Materials and Nanocomposites from Metal-Organic Frameworks, Adv. Mater., 29 (2017).

[30] R. Lippi, S.C. Howard, H. Barron, C.D. Easton, I.C. Madsen, L.J. Waddington, C. Vogt, M.R. Hill, C.J. Sumby, C.J. Doonan, D.F. Kennedy, Highly active catalyst for CO_2 methanation derived from a metal organic framework template, J. Mater. Chem. A, 5 (2017) 12990-12997.

[31] V.P. Santos, T.A. Wezendonk, J.J.D. Jaen, A.I. Dugulan, M.A. Nasalevich, H.U. Islam, A. Chojecki, S. Sartipi, X. Sun, A.A. Hakeem, A.C.J. Koeken, M. Ruitenbeek, T. Davidian, G.R. Meima, G. Sankar, F. Kapteijn, M. Makkee, J. Gascon, Metal organic framework-mediated synthesis of highly active and stable Fischer-Tropsch catalysts, Nat. Commun., 6 (2015) 6451.

[32] H. Wang, M. Liu, S. Guo, Y. Wang, X. Han, Y. Bai, Efficient oxidation of o-xylene over CeO2 catalyst prepared from a Ce-MOF template: The promotion of K+ embedding substitution, Mol. Catal., 436 (2017) 120-127.

[33] D. Xu, Y. Pan, M. Chen, Q. Pan, L. Zhu, M. Xue, D. Zhang, Q. Fang, S. Qiu, Synthesis and application of a MOF-derived Ni@C catalyst by the guidance from an in situ hot stage in TEM, RSC Adv., 7 (2017) 26377-26383.

[34] D. Chen, M. Huang, S. He, S. He, L. Ding, Q. Wang, S. Yu, S. Miao, Ru-MOF enwrapped by montmorillonite for catalyzing benzene hydrogenation, Appl. Clay Sci., 119 (2016) 109-115.

[35] Z. Wang, X. Li, Y. Yang, Y. Cui, H. Pan, Z. Wang, B. Chen, G. Qian, Highly dispersed beta-NiS nanoparticles in porous carbon matrices by a template metal-organic framework method for lithium-ion cathode, J. Mater. Chem. A, 2 (2014) 7912-7916.

[36] M.J. Katz, Z.J. Brown, Y.J. Colón, P.W. Siu, K.a. Scheidt, R.Q. Snurr, J.T. Hupp, O.K. Farha, A facile synthesis of UiO-66, UiO-67 and their derivatives, Chem. Commun., 49 (2013) 9449-9451.

[37] B. Schmitt, C. Bronnimann, E.F. Eikenberry, F. Gozzo, C. Hormann, R. Horisberger, B. Patterson, Mythen detector system, Nucl. Instrum. Methods Phys. Res., Sect. A, 501 (2003) 267-272.

[38] I.C. Madsen, N.V.Y. Scarlett, R. Kleeberg, K. Knorr, Quantitative phase analysis, in: C.J. Gilmore, J.A. Kaduk, H. Schenk (Eds.) International Tables for Crystallography Volume H: Powder diffraction2019, pp. 344-373.

[39] Topas V5: General Profile and Structure Analysis Software for Powder Diffraction Data, Bruker AXS GmbH, Karlsruhe, Germany, 2012.

[40] S. Sharifian, M. Miltner, M. Harasek, Thermodynamic and Kinetic Based Simulation Approach to CO2 and CO Methane Hydrogenation, Chem. Eng. Trans., 52 (2016) 565-570.

[41] R.P.M.B. do Amaral, Kinetics of CO2 methanation over a Ni/alumina industrial catalyst, Chemical engineering, Instituto Superior Técnico, 2016.

[42] D. Sun, D.S.A. Simakov, Thermal management of a Sabatier reactor for CO2 conversion into CH4: Simulation-based analysis, J. CO2 Util., 21 (2017) 368-382.

[43] J. Kehres, J.G. Jakobsen, J.W. Andreasen, J.B. Wagner, H. Liu, A. Molenbroek, J. Sehested, I. Chorkendorff, T. Vegge, Dynamical Properties of a Ru/MgAl2O4 Catalyst during Reduction and Dry Methane Reforming, J. Phys. Chem. C, 116 (2012) 21407-21415.

[44] M.R. Smith, S.W. Hedges, R. LaCount, D. Kern, N. Shah, G.P. Huffman, B. Bockrath, Selective oxidation of single-walled carbon nanotubes using carbon dioxide, Carbon, 41 (2003) 1221-1230.

[45] O.A. Graeve, Zirconia, in: J.F. Shackelford, R.H. Doremus (Eds.) Ceramic and Glass Materials: Structure, Properties and Processing, Springer US, Boston, MA, 2008, pp. 169-197.

[46] A. Navrotsky, L. Benoist, H. Lefebvre, Direct Calorimetric Measurement of Enthalpies of Phase Transitions at 2000°–2400°C in Yttria and Zirconia, J. Am. Ceram. Soc., 88 (2005) 2942-2944.

[47] A. Solis-Garcia, J.C. Fierro-Gonzalez, Mechanistic Insights into the CO2 Methanation Catalyzed by Supported Metals: A Review, J. Nanosci. Nanotechnol., 19 (2019) 3110-3123.

[48] H. Habazaki, M. Yamasaki, B.-P. Zhang, A. Kawashima, S. Kohno, T. Takai, K. Hashimoto, Co-methanation of carbon monoxide and carbon dioxide on supported nickel and cobalt catalysts prepared from amorphous alloys, Appl. Catal., A, 172 (1998) 131-140.

[49] M. Yamasaki, H. Habazaki, K. Asami, K. Izumiya, K. Hashimoto, Effect of tetragonal ZrO_2 on the catalytic activity of Ni/ZrO_2 catalyst prepared from amorphous Ni–Zr alloys, Catal. Commun., 7 (2006) 24-28.

[50] J.B. DeCoste, G.W. Peterson, H. Jasuja, T.G. Glover, Y.G. Huang, K.S. Walton, Stability and degradation mechanisms of metal-organic frameworks containing the Zr6O4(OH)(4) secondary building unit, J. Mater. Chem. A, 1 (2013) 5642-5650.

[51] E. Djurado, P. Bouvier, G. Lucazeau, Crystallite Size Effect on the Tetragonal-Monoclinic Transition of Undoped Nanocrystalline Zirconia Studied by XRD and Raman Spectrometry, J. Solid State Chem., 149 (2000) 399-407.

[52] A.S. Barnard, R.R. Yeredla, H. Xu, Modelling the effect of particle shape on the phase stability of ZrO2nanoparticles, Nanotechnology, 17 (2006) 3039-3047.

[53] M. Vandichel, J. Hajek, F. Vermoortele, M. Waroquier, D.E. De Vos, V. Van Speybroeck, Active site engineering in UiO-66 type metal–organic frameworks by intentional creation of defects: a theoretical rationalization, CrystEngComm, 17 (2015) 395-406.

[54] S.J. Gurman, EXAFS studies in materials science, J. Mater. Sci., 17 (1982) 1541-1570.

[55] J.J. Gao, Y.L. Wang, Y. Ping, D.C. Hu, G.W. Xu, F.N. Gu, F.B. Su, A thermodynamic analysis of methanation reactions of carbon oxides for the production of synthetic natural gas, RSC Adv., 2 (2012) 2358-2368.

[56] H.V. Thang, S. Tosoni, L. Fang, P. Bruijnincx, G. Pacchioni, Nature of Sintering-Resistant, Single-Atom Ru Species Dispersed on Zirconia-Based Catalysts: A DFT and FTIR Study of CO Adsorption, Chemcatchem, 10 (2018) 2634-2645.

Figure
Click here to download high resolution image

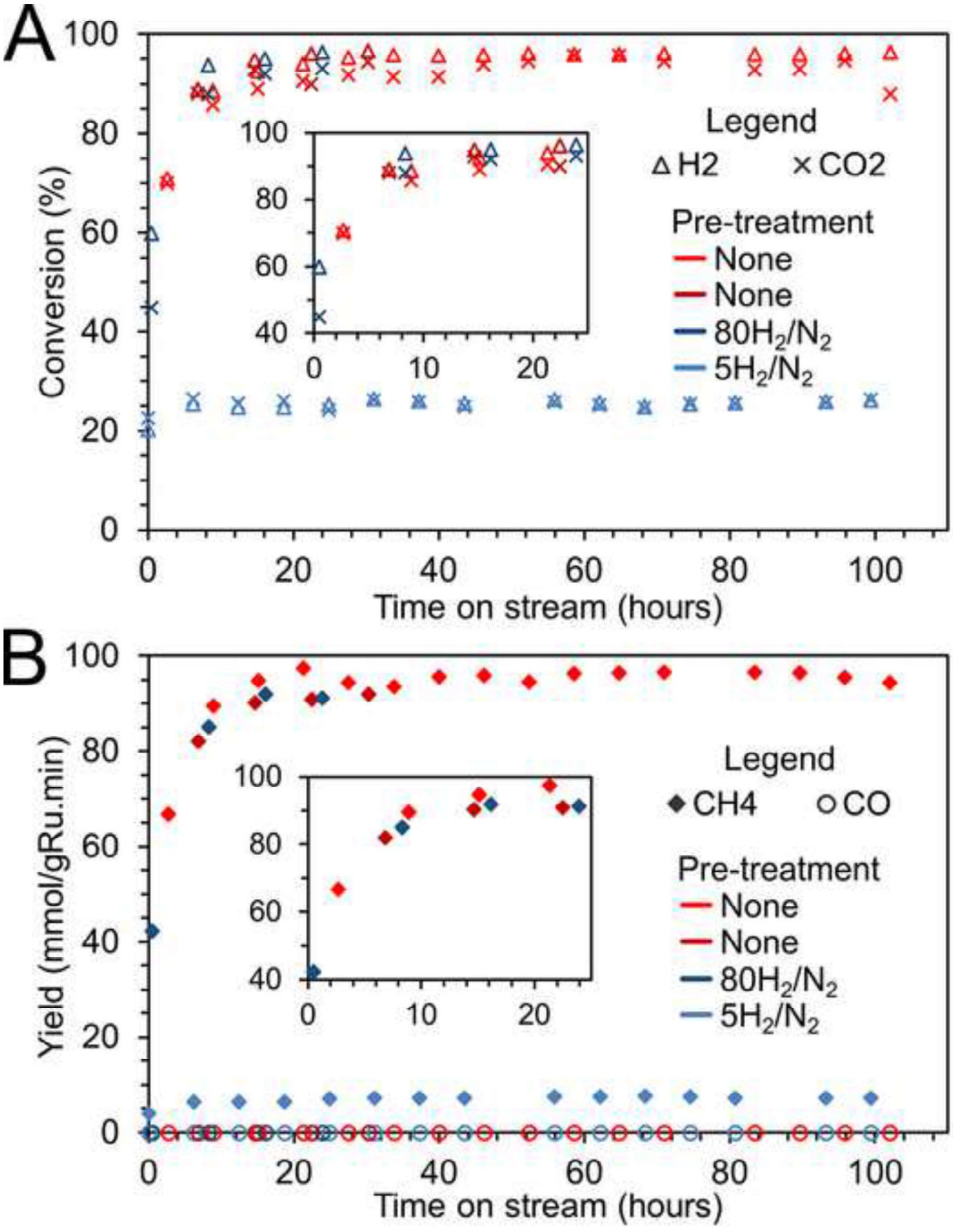

Figure
Click here to download high resolution image

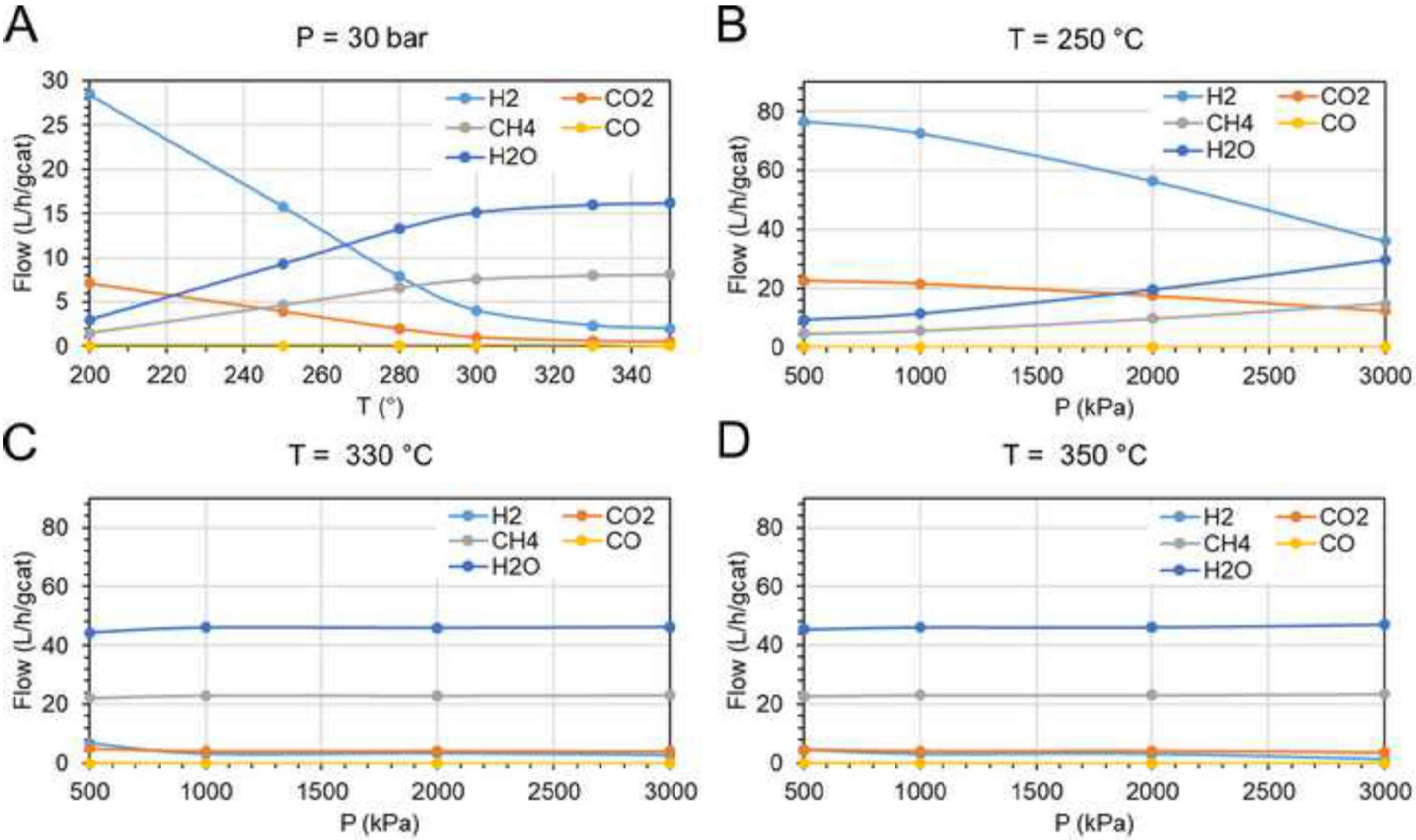

Figure
Click here to download high resolution image

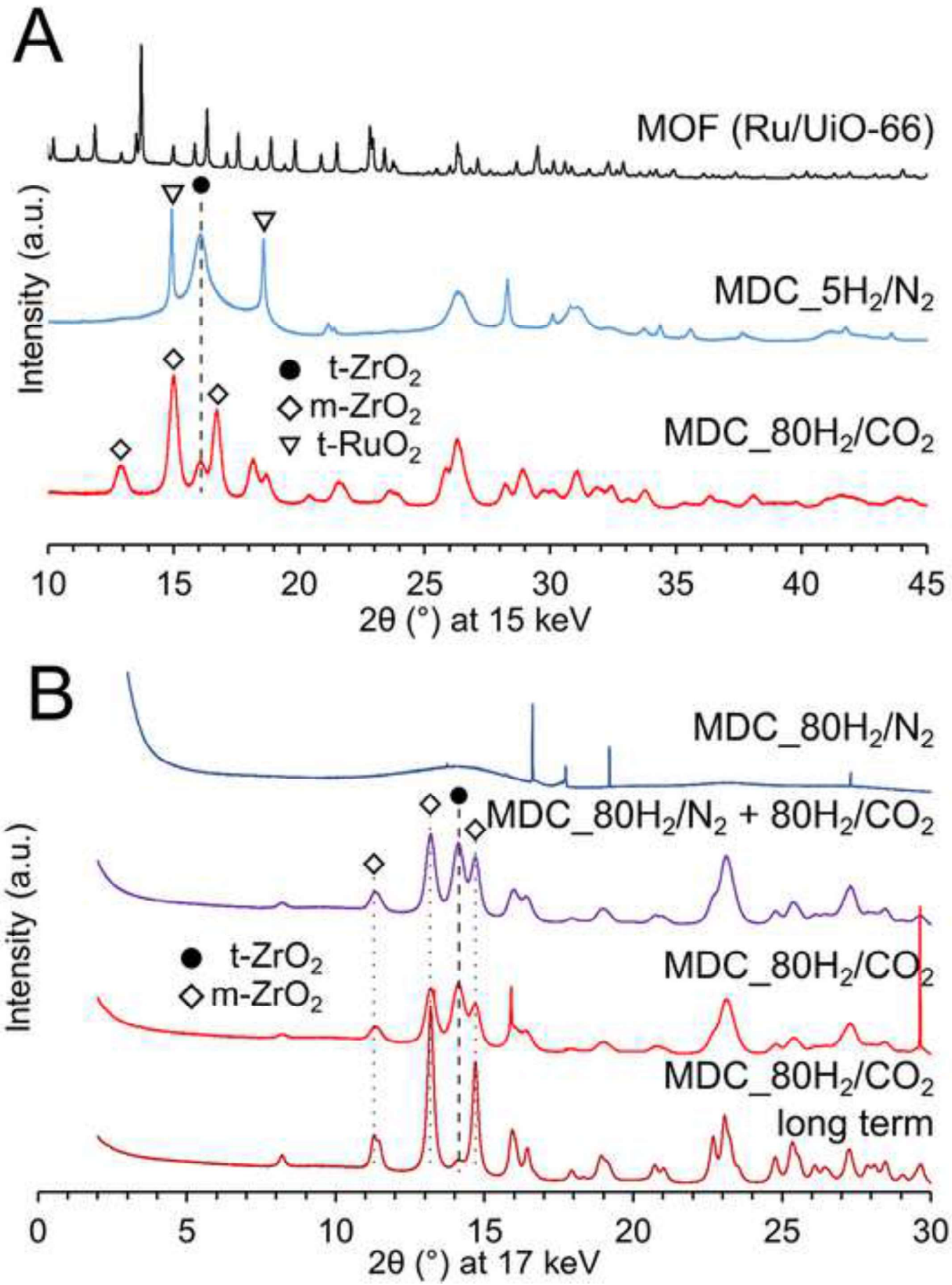

Figure

Click here to download high resolution image

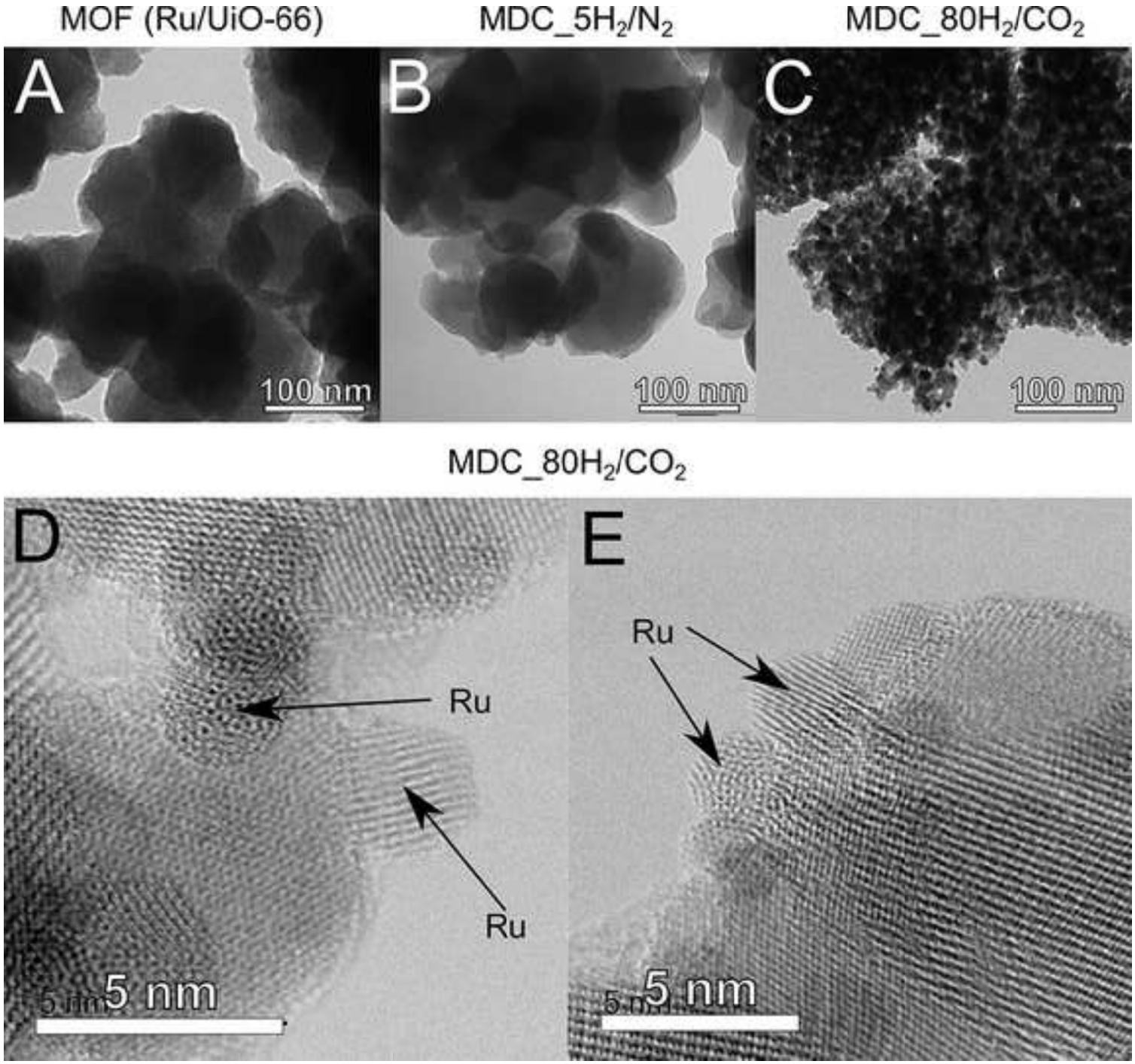

Figure
Click here to download high resolution image

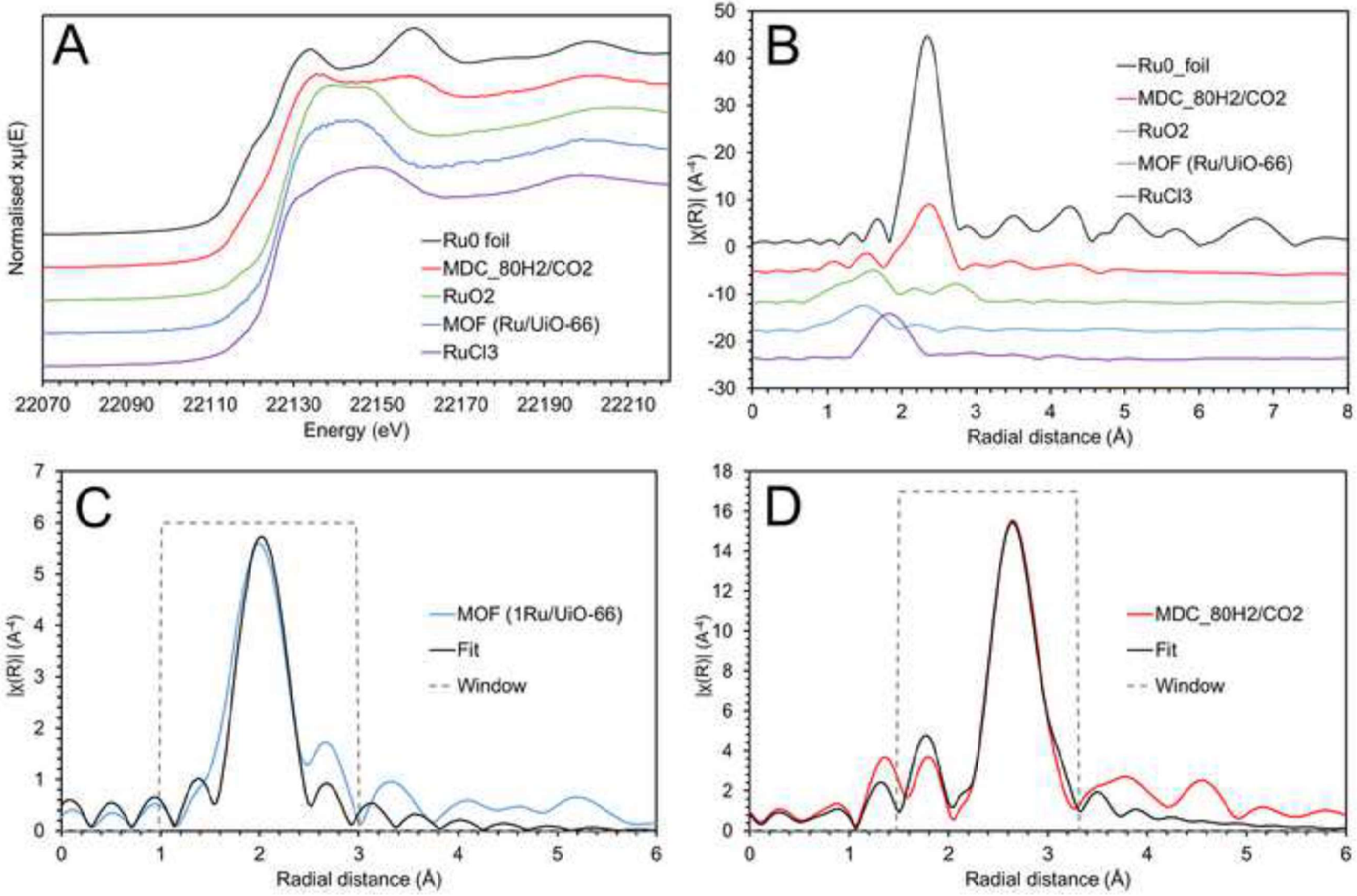

Figure
Click here to download high resolution image

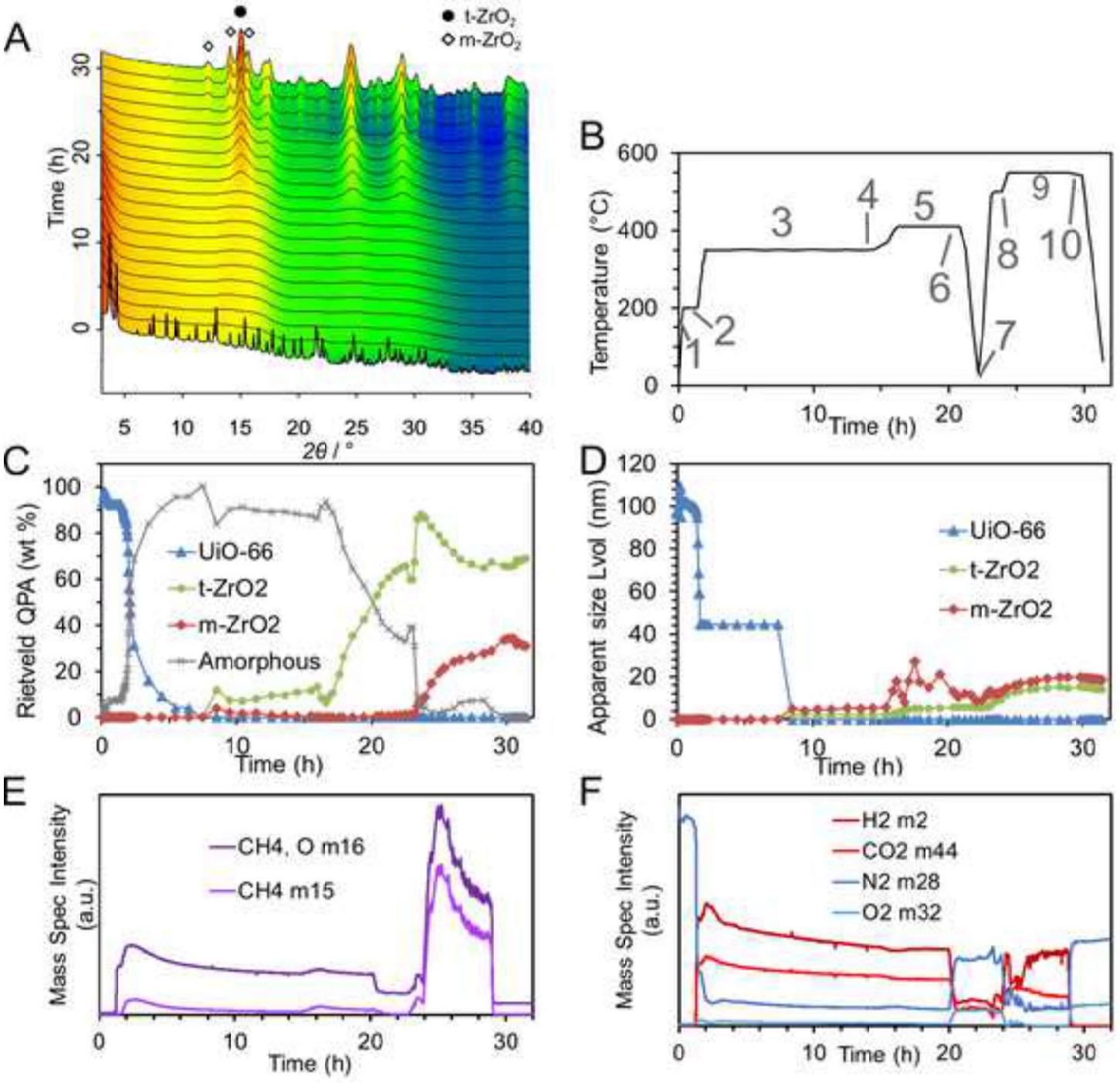

Figure
Click here to download high resolution image

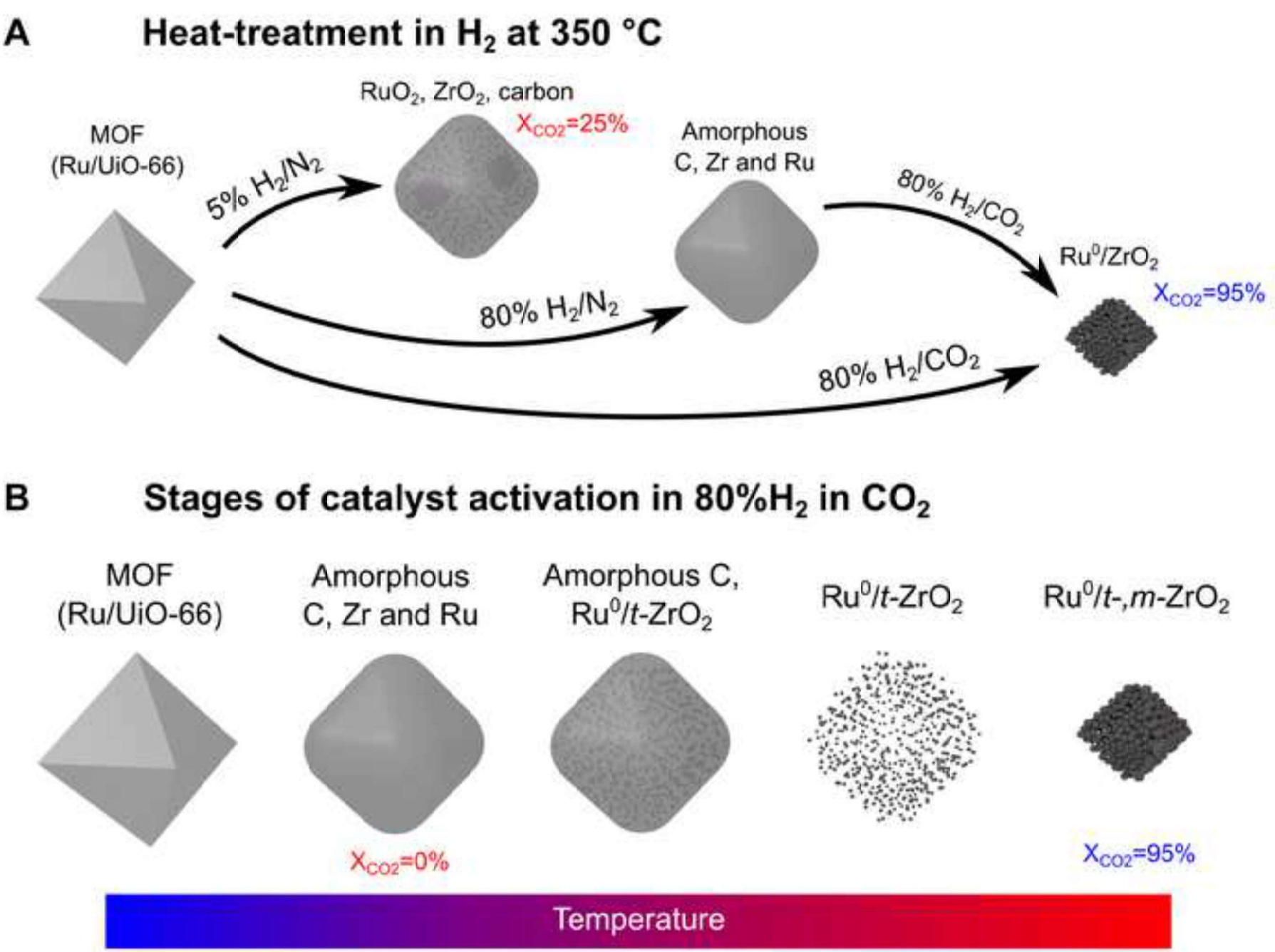

Supporting information of

Unveiling the structural transitions during activation of a CO_2 methanation catalyst Ru^0/ZrO_2 synthesised from a MOF precursor

Renata Lippi,*[1,2,3] Anita M. D'Angelo,[4] Chaoen Li,[3] Shaun C. Howard,[1] Ian C. Madsen,[5] Karen Wilson,[6] Adam Lee,[6] Christopher J. Sumby,[2] Christian J. Doonan,[2] Jim Patel,[3] Danielle Kennedy[1]

[1] CSIRO Manufacturing, Clayton VIC, Australia
[2] Department of Chemistry and Centre for Advanced Nanomaterials, The University of Adelaide, Adelaide SA, Australia
[3] CSIRO Energy, Clayton North VIC, Australia
[4] Australian Synchrotron, Clayton VIC, Australia
[5] CSIRO Minerals, Clayton VIC, Australia
[6] Department of Applied Chemistry and Environmental Sciences, RMIT, Melbourne VIC, Australia

*Corresponding author: renata.lippi@csiro.au

1. Synthesis

1.1 Materials

Zirconium (IV) chloride anhydrous ($ZrCl_4$) 99.99% Sigma Aldrich (Australia), ruthenium(III) chloride trihydrate ($RuCl_3$•$3H_2O$) 99% PMO Pty Ltd (Australia), terephthalic acid (H2BDC) 99% Acros Organics (Great Britain), N-N-dimethylformamide (DMF) 99.8% Merck Pty. Ltd. (Australia), diethyl ether (DEE) for analysis Merck Pty. Ltd. (Australia), hydrochloric acid (HCl) 32% Merck Pty. Ltd. (Australia).

1.2 MOF synthesis

UiO-66 synthesis was based on the procedure reported by Katz *et al.* [1]. In a glass vial, terephthalic acid (623 mg, 3.75 mmol) was dissolved in 50 mL of N-N-dimethylformamide (DMF). In a second glass vial, $ZrCl_4$ (629 mg, 2.7 mmol) and 5 mL of HCl were dissolved in 25 mL of DMF, the latter vial was sonicated for 20 min to ensure complete dissolution. Next, the $ZrCl_4$ solution was mixed with the organic ligand solution and the vial sealed with a Teflon lined screw cap and placed in an aluminium heating block at 80 °C for 48 hours. The resulting precipitate was centrifuged, washed (4x10 mL DMF and 2x10 mL of ethanol) and dried at 110 °C for 48 hours to yield UiO-66.

Table S1: Quantities used for the synthesis of the MOFs.

MOF sample	Ligand	Ligand (mmol)	Ligand (mg)	Metal precursor	Metal precursor (mmol)	Metal precursor (mg)	Modulator	Modulator volume (mL)	DMF (mL)
UiO-66	H_2BDC	3.75	623	$ZrCl_4$	2.7	629	HCl	5	75

1.3 Post-synthetic modification of UiO-66

Impregnation of Ru on UiO-66 was carried out via incipient wetness impregnation previously reported [2]. Typically, 250 mg of UiO-66 was impregnated with an aqueous solution of $RuCl_3$ (6.5 mg of $RuCl_3 \cdot 3H_2O$ and 345 µL of H_2O) via incipient wetness impregnation, to yield the catalyst precursor 1wt%Ru/UiO-66.

Table S2: Quantities used for the impregnation of UiO-66 with different loadings of Ru.

Sample	Ru loading (wt%)	Mass $RuCl_3.3H_2O$ (mg)	Mass support UiO-66 (mg)	H_2O vol. (µL)
1.00%Ru/UiO-66	1.00	6.5	250	345

2. Catalysis

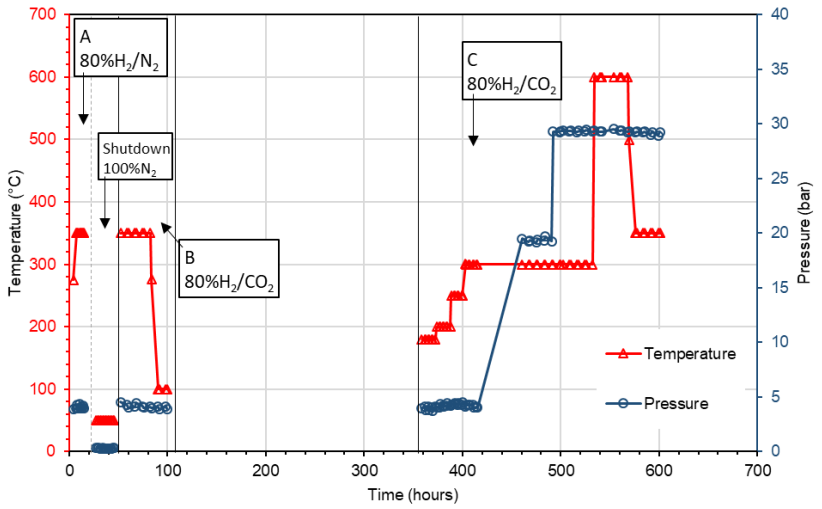

Figure S1: Gas composition and temperature/pressure profiles for catalysis experiment studying the effect of high H_2 concentration in MOF-templating. The vertical solid black lines indicate rig shutdown to remove and replace samples (this involved cooling down to room temperature, ambient pressure and exposure of samples to air). The vertical dashed line indicated the rig was shut down, but the samples kept in the rig at 50 °C under pure N_2 gas flow.

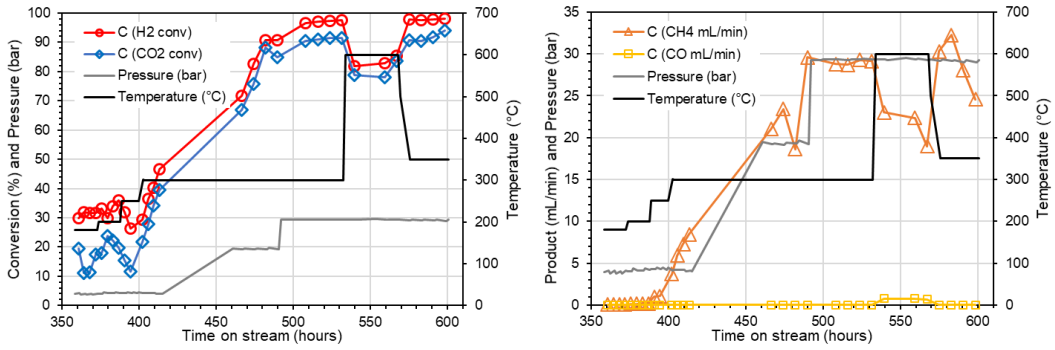

Figure S2: Reaction conditions and results for the long term (250 hours) experiment that yielded sample “Ru/ZrO2-80H2/CO2 long term”. The experiment was paused from 415 until 565 hours, during this period the samples were kept under a flow of inert gas at the temperature indicated.

3. TGA

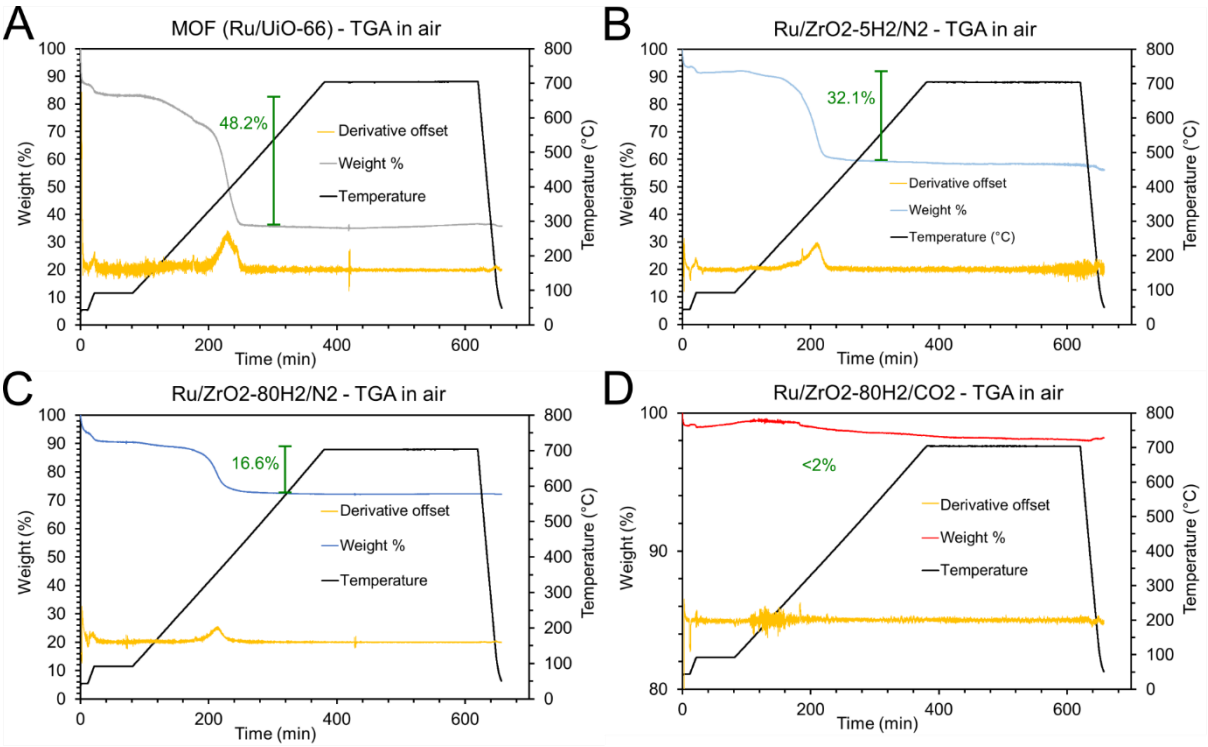

Figure S3: Thermogravimetric analysis results for (A) MOF, (B) Ru/ZrO2-5H2/N2, (C) Ru/ZrO2-80H2/N2 and (D) Ru/ZrO2-80H2/CO2.

4. X-ray absorption spectroscopy

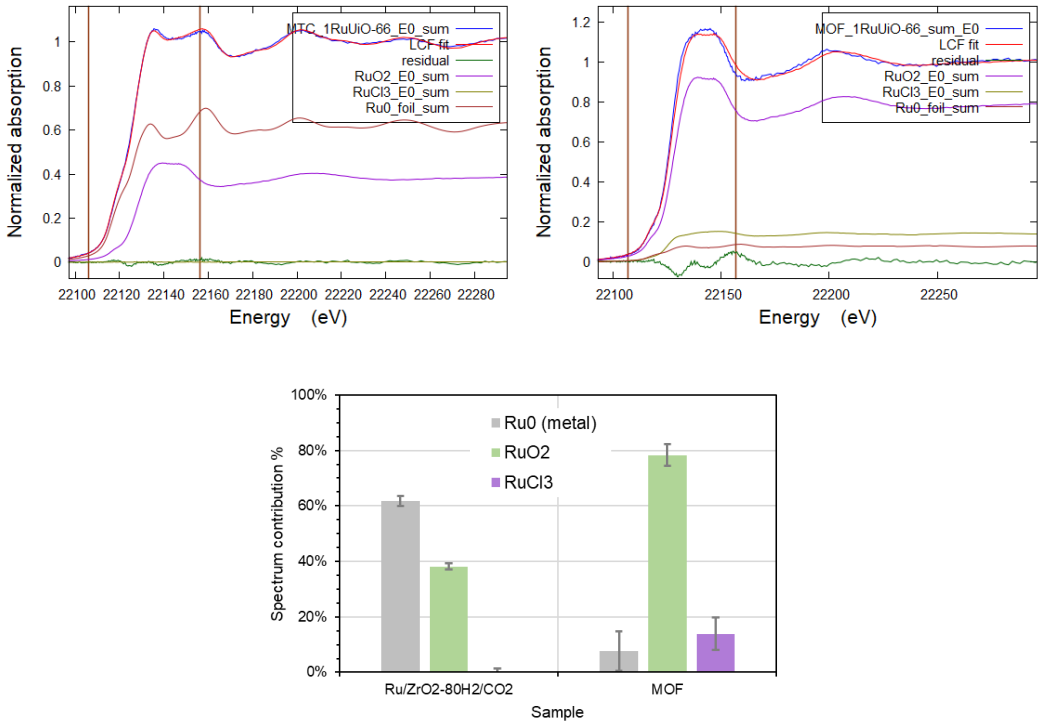

Figure S4: XANES spectra for MOF-templated catalyst (top left) and for its precursor 1Ru/UiO-66 in pristine form (top right) and linear combination of standards Ru^0 foil, RuO_2 and $RuCl_3$ to fit the samples spectra (bottom).

Table S3: Values of the spline range in k used for EXAFS analyses.

Sample	k min	k max
Ru^0 foil	3	13.9
$RuCl_3$	3	10.6
RuO_2	3	12.4
MOF	3	10.1
Ru/ZrO2-80H2/CO2	3	12

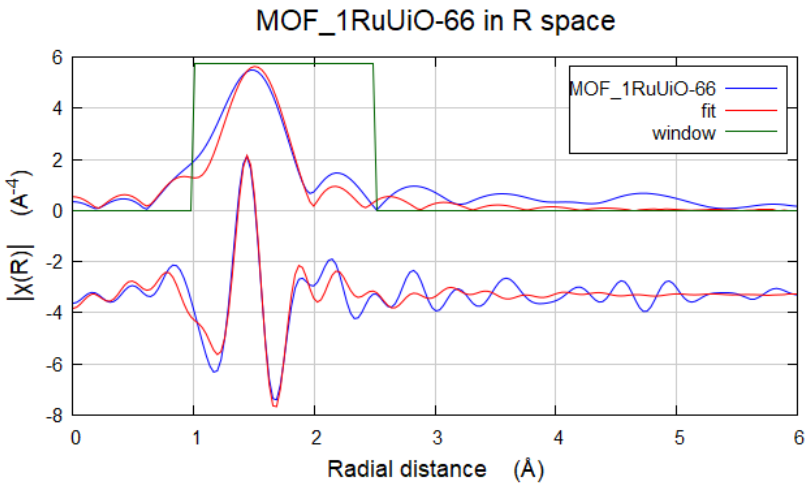

Figure S5: k^3-weighted Fourier transform EXAFS spectra for MOF (Ru/UiO-66) and fit with Ru-O path contribution. Magnitude (top) and imaginary (bottom) parts are presented.

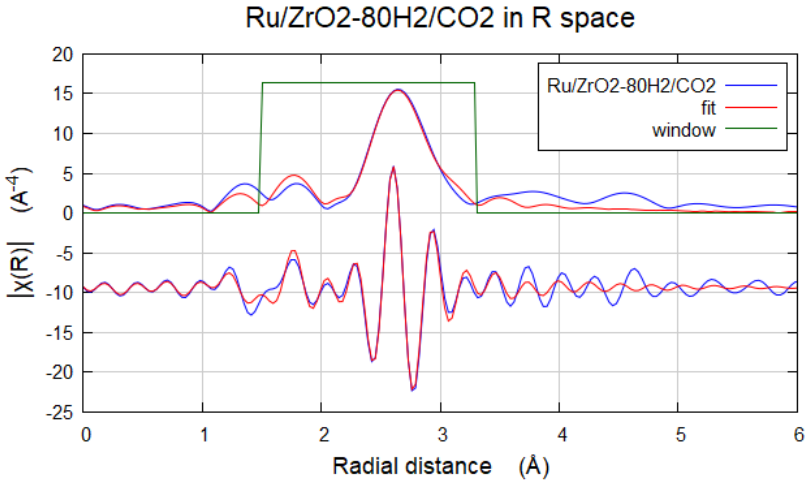

Figure S6: k^3-weighted Fourier transform EXAFS spectra for MOF-derived catalyst (Ru/ZrO2-80H2/CO2) and fit with Ru-Ru and Ru-O paths contributions. Magnitude (top) and imaginary (bottom) parts are presented.

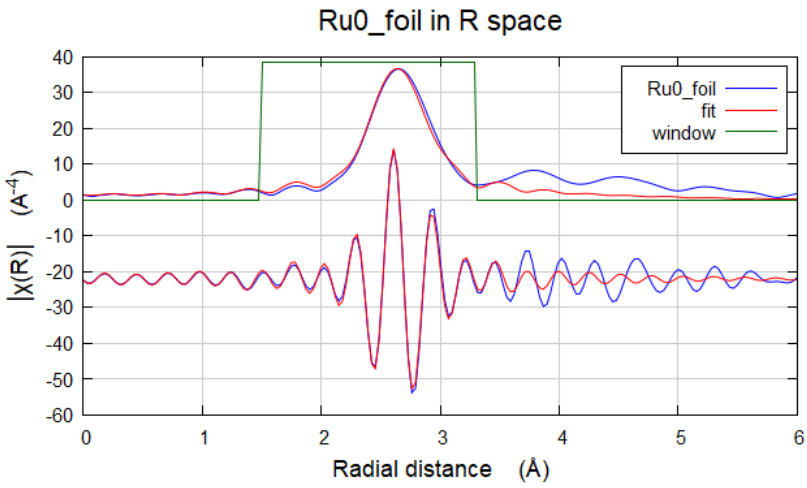

Figure S7: k^3-weighted Fourier transform EXAFS spectra for Ru^0 foil and fit with Ru-Ru and path contribution. Magnitude (top) and imaginary (bottom) parts are presented.

5. Powder X-ray diffraction

5.1 Laboratory PXRD

The XRD pattern of UiO-66 as synthesised was obtained on a Bruker D8 Advance X-ray Diffractometer operating under CuKα radiation (40kV, 40mA) equipped with a LynxEye detector. Flat packed samples were scanned over the 2θ range 3.5° to 130° with a step size of 0.02° and a count time of 0.4 second per step. The data were re-plotted at E = 15 keV.

Powder X-ray diffraction patterns were collected with synchrotron and with laboratory source X-rays. The X-ray source and respective energy for each image presented in the manuscript are described below:

- Figure 3A plotted at 15 keV, collected as below
    - **MOF(Ru/UiO-66)** Synchrotron at 15 keV
    - **Ru/ZrO2-5H2/N2** Synchrotron at 15 keV
    - **Ru/ZrO2-80H2/CO2** Synchrotron at 16 keV
- Figure 3B all patterns, synchrotron at 17 keV
- Figure S8:
    - **UiO-66** Cu radiation 8.04 keV
    - UiO-66 after treatment in 5% H_2/N_2 Synchrotron at 15 keV
    - UiO-66 after treatment in 80% H_2/N_2 Synchrotron at 16 keV
- Figure 6 (in operando): Synchrotron 16 keV

For comparison of PXRD patterns at the same energy, the patterns displayed in Figure 3A and Figure S8 which were not collected at 15 keV were plotted for E = 15 keV using Eq. 6:

Planck–Einstein relation

$$E = h\nu \Rightarrow E = h\frac{c}{\lambda} \quad \text{(Eq. 1)}$$

$$\begin{cases} E_1 = h\frac{c}{\lambda_1} \\ E_2 = h\frac{c}{\lambda_2} \end{cases} \Rightarrow E_1\lambda_1 = E_2\lambda_2 \Rightarrow \frac{E_1}{E_2} = \frac{\lambda_2}{\lambda_1} \quad \text{(Eq. 2)}$$

Bragg's law

$$n\lambda = 2d \cdot sin\theta \quad \text{(Eq. 3)}$$

$$d = \frac{n\lambda}{2 \cdot sin\theta} \Rightarrow d_1 = d_2 \Rightarrow \frac{n\lambda_1}{2 \cdot sin\theta_1} = \frac{n\lambda_2}{2 \cdot sin\theta_2} \Rightarrow \frac{\lambda_2}{\lambda_1} = \frac{sin(\theta_2)}{sin(\theta_1)} \quad \text{(Eq. 4)}$$

Combining Eq. 2 and 4

$$\frac{E_1}{E_2} = \frac{\lambda_2}{\lambda_1} = \frac{sin(\theta_2)}{sin(\theta_1)} \Rightarrow sin\left(\frac{2\theta_2}{2}\right) = sin\left(\frac{2\theta_1}{2}\right) \cdot \frac{E_1}{E_2} \quad \text{(Eq. 5)}$$

$$2\theta_2 = sin^{-1}\left(sin\left(\frac{2\theta_1}{2}\right) \cdot \frac{E_1}{E_2}\right) \cdot 2 \quad \text{(Eq. 6)}$$

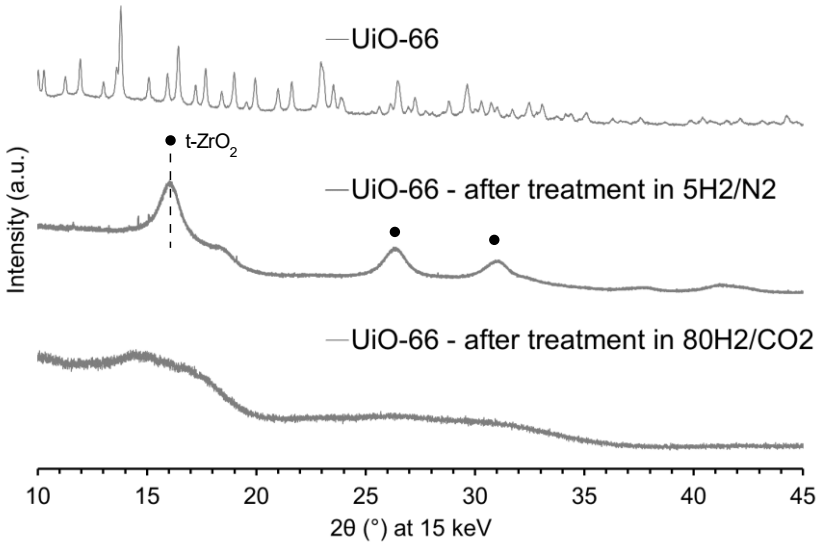

Figure S8: PXRD patterns for UiO-66 and its derived structures after heat-treatment under different atmospheres.

5.2 Rietveld refinement

Rietveld refinement is a least-squares method to refine a calculated model based on the observed pattern profile.[3] The method seeks to minimize the difference between observed and calculated patterns (R_wp). For the models to be calculated the structures and background functions should be manually defined and selected structural parameters and individual phase scale factor are refined. Here, the crystalline structures considered are: monoclinic ZrO_2, tetragonal ZrO_2 and UiO-66.[4] Parameters refined include: scale factor, unit cell parameters, and Lvol or LvolIB (Lvol values were extracted from peak width and shape using Integral breadth) [5].

5.2.1 Amorphous phases fitting

Using the pattern of the first dataset, which presented the starting materials, UiO-66, in the most crystalline form, the capillary background was refined using six pseudo-voigt peaks. Once the capillary background was refined for this pattern, the relative intensities of this *capillary phase* were fixed and associated with a *scale factor*, capable of multiplying intensity of the peaks while keeping the relative intensities constant. Next, the first completely amorphous dataset pattern was selected and refined only with the capillary phase. A misfit between the calculated and observed data was observed, which was due to the amorphisation of the sample. To assign the contribution another phase was created by adding a total of five pseudo-voigt peaks and they were refined to improve the fit of the phase. Once the relative intensities were adequate to comprise the amorphous phase, the relative intensities of these 5 peaks were fixed and another scale factor was assigned to the *amorphous phase*. The peaks group of the amorphous phase was verified on other datasets of the amorphous region before the batch refinement.

5.2.2 Batch Rietveld refinement

As over 700 datasets were collected in total, 93 patterns were selected to be representative of the total phase transition. Where phase transitions were observed, more datasets were selected and where the phase was stable, less datasets were selected for the analysis. In total 5 phases were refined: UiO-66, monoclinic ZrO_2, tetragonal ZrO_2, amorphous peak phase and capillary peak phase. The datasets were evaluated for the presence of crystalline phase. Accordingly, datasets collected in the first 8 hours, were refined for UiO-66, amorphous peak phase and capillary peak phase, whereas datasets collected after the first 8 hours of experiment were refined for m-ZrO_2, t-ZrO_2, amorphous peak phase and capillary peak phase. The datasets were refined in sequence using the launch mode of TOPAS V5.[6] The refined values of the previous dataset were used as starting point for the refinement of the subsequent dataset. An example of input file is presented at the end of this document.

5.2.3 Indirect quantitative phase analysis

Direct quantitative phase analysis via Rietveld refinement is only possible for crystalline phases [7], however, as the amorphous phase contribution is observable and the sample is contained within the capillary (i.e. no material added or removed), the indirect quantitative phase analysis of this amorphous phase is possible. In this work, the maximum scale factor (Figure S9 A) observed for the

amorphous phase was defined as 100 wt% amorphous phase content, with proportional values for other values of scale factor. The results from the direct quantitative phase analysis of the crystalline phases (UiO-66, m-ZrO_2 and t-ZrO_2) were considered for the remaining phases (i.e. not-amorphous content). When considering the crystalline phases, misquantification of phases was noted due to the amorphisation of the sample. Apparent crystallite sizes (Lvol-IB) close to the minimum limit are evidence of the misquantification (Figure S9 C and D). Figure S9 C shows the independent quantification of the amorphous phase and the crystalline phases and Figure S9 D shows the apparent crystallite size (Lvol-IB) constant and value on the minimum limit.

Therefore, the quantification of the phases, including the amorphous phase was calculated using the following equation:

$$W_{\%_{Crys\ phase\ real}} = W_{\%_{Crys\ phase\ Rietveld}} \cdot \left(\frac{100 - \frac{SF_{Amorphous} \cdot 100}{SF_{Amorphous\ MAX}}}{100} \right)$$

Where:

- $W_{\%_{Crys\ phase\ real}}$ is the weight percentage considering the amorphous phase, presented in Figure 6C;
- $W_{\%_{Crys\ phase\ Rietveld}}$ is the weight percent of a crystalline phase calculated directly via Rietveld refinement (Figure S9 C);
- $SF_{Amorphous\ MAX}$ is the maximum scale factor observed for the amorphous phase (1.08), where the sample is completely amorphous;
- $SF_{Amorphous}$ is the scale factor for the respective dataset.

No other manipulation was performed in the data.

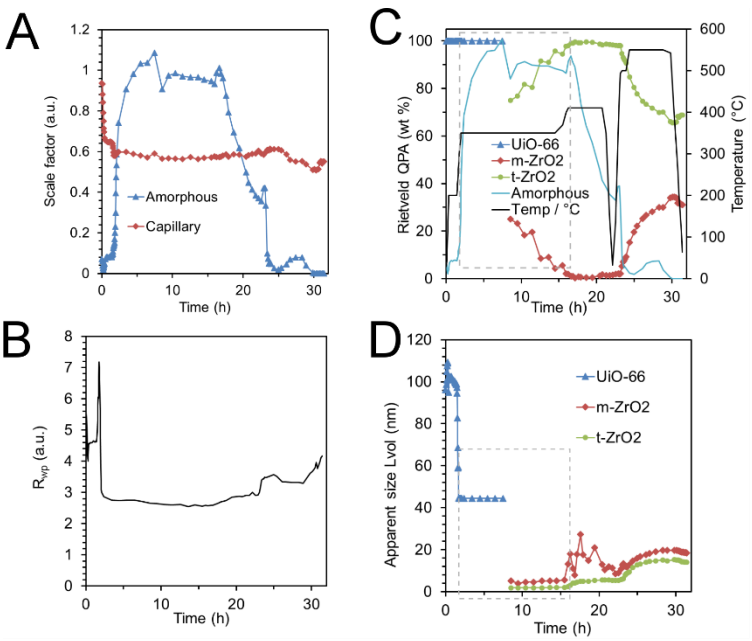

Figure S9: Rietveld refinement results: A) Scale factors for the two fitted amorphous phases: capillary and MOF-derived amorphous phase; B) Weighted profile R (R_{wp}); C) Quantitative phase analysis as obtained from the refinement; D) Apparent crystallite size (Lvol).

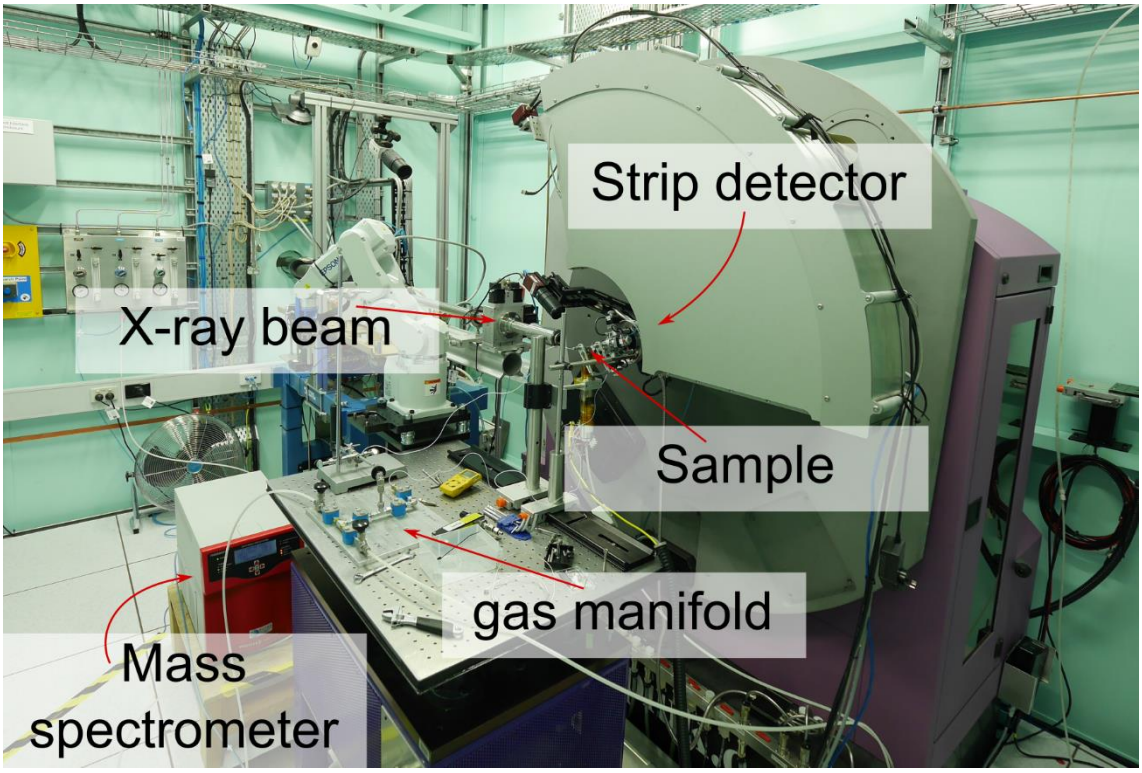

Figure S10: Photo of *in operando* PXRD set-up.

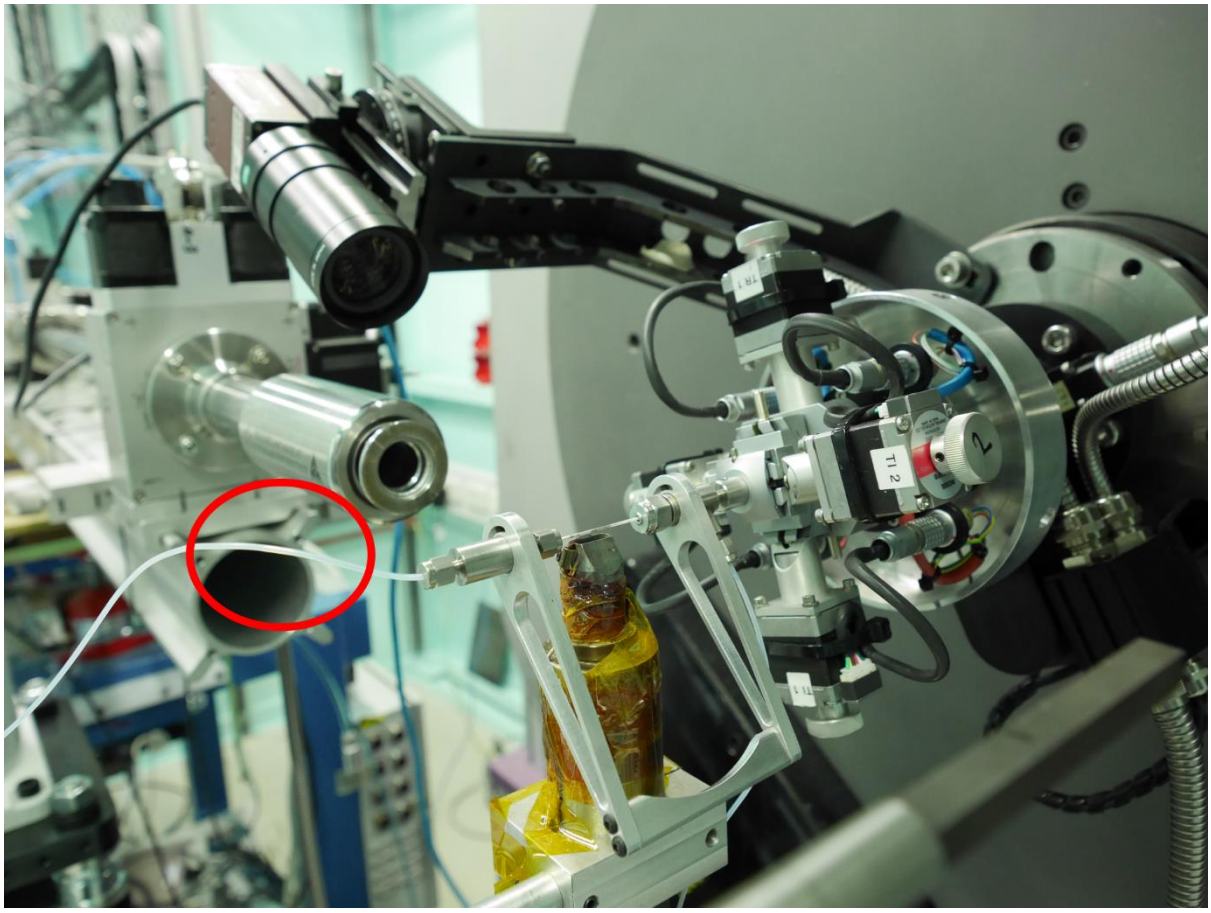

Figure S11: Photo of water drop in the effluent gas nylon tubing, affecting mass spectrometry data collection.

6. References

[1] M.J. Katz, Z.J. Brown, Y.J. Colón, P.W. Siu, K.a. Scheidt, R.Q. Snurr, J.T. Hupp, O.K. Farha, A facile synthesis of UiO-66, UiO-67 and their derivatives, Chem. Commun., 49 (2013) 9449-9451.
[2] R. Lippi, S.C. Howard, H. Barron, C.D. Easton, I.C. Madsen, L.J. Waddington, C. Vogt, M.R. Hill, C.J. Sumby, C.J. Doonan, D.F. Kennedy, Highly active catalyst for CO_2 methanation derived from a metal organic framework template, J. Mater. Chem. A, 5 (2017) 12990-12997.
[3] H. Rietveld, A profile refinement method for nuclear and magnetic structures, J. Appl. Crystallogr., 2 (1969) 65-71.
[4] L. Valenzano, B. Civalleri, S. Chavan, S. Bordiga, M.H. Nilsen, S. Jakobsen, K.P. Lillerud, C. Lamberti, Disclosing the Complex Structure of UiO-66 Metal Organic Framework: A Synergic Combination of Experiment and Theory, Chem. Mater., 23 (2011) 1700-1718.
[5] M. Leoni, Domain size and domain-size distributions, in: C.J. Gilmore, J.A. Kaduk, H. Schenk (Eds.) International Tables for Crystallography Volume H: Powder diffraction 2019, pp. 524-537.
[6] Topas V5: General Profile and Structure Analysis Software for Powder Diffraction Data, Bruker AXS GmbH, Karlsruhe, Germany, 2012.
[7] I.C. Madsen, N.V.Y. Scarlett, R. Kleeberg, K. Knorr, Quantitative phase analysis, in: C.J. Gilmore, J.A. Kaduk, H. Schenk (Eds.) International Tables for Crystallography Volume H: Powder diffraction 2019, pp. 344-373.